REPUBLIC OF TURKEY

YILDIZ TECHNICAL UNIVERSITY

GRADUATE SCHOOL OF NATURAL AND APPLIED SCIENCES

# MICROFLUIDIC SYSTEM DEVELOPMENT FOR DETECTION OF SINGLE-CELL MECHANICAL PROPERTIES

**Gizem AYDEMIR**

MASTER OF SCIENCE THESIS

Department of Mechatronics Engineering

Mechatronics Engineering Program

Advisor

Asst. Prof. Dr. Huseyin Uvet

Co-Advisor

Prof. Dr. Ali Kosar

August, 2020

REPUBLIC OF TURKEY

YILDIZ TECHNICAL UNIVERSITY

GRADUATE SCHOOL OF NATURAL AND APPLIED SCIENCES

# MICROFLUIDIC SYSTEM DEVELOPMENT FOR DETECTION OF SINGLE-CELL MECHANICAL PROPERTIES

A thesis submitted by Gizem AYDEMIR in partial fulfillment of the requirements for the degree of MASTER OF SCIENCE is approved by the committee on 07.08.2020 in Department of Mechatronics Engineering, Mechatronics Engineering Program.

| Asst. Prof. Dr. Huseyin UVET | Prof. Dr. Ali KOSAR |
|---|---|
| Yıldız Technical University | Sabanci University |
| Advisor | Co-Advisor |

**Approved By the Examining Committee**

Asst. Prof. Dr. Huseyin UVET, Advisor
Yıldız Technical University _____

Prof. Dr. Ali KOSAR, Co-Advisor
Sabanci University _____

Assoc. Prof. Dr. Kadir ERKAN, Member
Yıldız Technical University _____

I hereby declare that I have obtained the required legal permissions during data collection and exploitation procedures, that I have made the in-text citations and cited the references properly, that I haven't falsified and/or fabricated research data and results of the study and that I have abided by the principles of the scientific research and ethics during my Thesis Study under the title of Microfluidic System Development For Detection Of Single-Cell Mechanical Properties supervised by my supervisor, Asst. Prof. Dr. Huseyin UVET and my co-supervisor Prof. Dr. Ali KOSAR. In the case of a discovery of false statement, I am to acknowledge any legal consequence.

Gizem AYDEMIR

Signature

This study was supported by the Scientific and Technological Research Council of Turkey (TUBITAK) Grant No: 116E743 and scholarship through BİDEB 2210-C programme.

*Dedicated to my lovely family*

# ACKNOWLEDGEMENTS

I sincerely want to thank my advisor, Dr. Huseyin Uvet, who taught me the meaning of interdisciplinary science. I cannot thank enough for his help, understanding, and supervision.

Another thank is to my co-advisor Prof. Ali Kosar. In the realization of this work, whenever I consult him, he gives me his precious time and patiently and with great interest. His support during my Master was very valuable to me. Thank you very much sir for your help, patience, and belief in me.

I would like to thank my colleagues at the ASIL group for keeping my motivation high and improving the daily life both inside and outside the lab. I present my endless thanks to my precious friends, Rahmetullah Varol, Sevde Omeroglu, and Ali Anıl Demircali, who constantly guide me in terms of subject, source, and method in my study and believe that they will be more successful in their future life.

This master thesis was financed by TUBITAK within the framework of "1003 program", which is a collaboration project of Yildiz Technical University, Marmara University, and Dokuz Eylul University. Endless gratitude and thanks to Prof. Yasemin Baspinar and Dr. Gizem Calibasi Kocal for their support in providing cancer cells and teaching me cell culture studies in this thesis. Another thanks to Dr. Gokhan Bora Esmer from Marmara University for his support in the imaging system used in the thesis. Also, I would like to thank Dr. Enes Oruc from Gebze Technical University, who provided me with access to the cleanroom for microfluidic system and micro-robot fabrication in the project.

I would like to thank all my other university professors for all the things they have gained during my university life and for the information that will make me a voice in the future.

Special thanks to Ilter Ozmen. Thank you very much for the ideas, technical support, and motivation you gave me during my Master. I have collected many memories that I could have fun and find peace during my Master. I am grateful for your patience, support, and belief in me.

Endless thanks to my lovely family, who brought and raised me in a way that knows the meaning of the respect of life and who supported me. My dear mother and dear father, you have always supported me no matter what decision I decide in my life, I cannot thank you enough. Another thank to my dear sisters Neslihan and Zubeyde for their support and nice coffee hours during the long working nights. My dear brother Mehmet, thank you for the talks on technical issues and for your enlightening ideas.

Gizem AYDEMİR

# TABLE OF CONTENTS

# LIST OF SYMBOLS

| | |
|---|---|
| $F_B$ | Buoyant force |
| $A_x$ | Cross sectional area of X-axis |
| $A_y$ | Cross sectional area of Y-axis |
| $A_z$ | Cross sectional area of Z-axis |
| $F_{g,x}$ | Diamagnetic force X-axis component |
| $F_{g,y}$ | Diamagnetic force Y-axis component |
| $F_{g,z}$ | Diamagnetic force Z-axis component |
| $F_r$ | Gravitational force |
| $\mathbf{H}$ | Magnetic field strength |
| $\mathbf{B}$ | Magnetic flux density |
| $F_{m,x}$ | Magnetic force X-axis component |
| $F_{m,y}$ | Magnetic force Y-axis component |
| $F_{m,z}$ | Magnetic force Z-axis component |
| $\chi$ | Magnetic insulation coefficient |
| $\mathbf{M}$ | Magnetization vector |
| $\mu_r$ | Relative permeability |

# LIST OF ABBREVIATIONS

| | |
|---|---|
| HCT-116 | Colon Cancer Cell Line |
| HUVEC | Human Umbilical Vein Endothelial Cells |
| MDA-MB-1 | Mammary Cancer Cell Line |
| MEMs | Micro-Electro-Mechanics |
| ONCO-DG-1 | Ovarian Cancer Cell Line |

# LIST OF FIGURES

# LIST OF TABLES

# ABSTRACT

## Microfluidic System Development for Detection of Single-Cell Mechanical Properties

Gizem AYDEMIR

Department of Mechatronics Engineering

Master of Science Thesis

Advisor: Asst. Prof. Dr. Huseyin UVET

Co-advisor: Prof. Dr. Ali KOSAR

This thesis aims to microfluidic systems have been developed to determine the mechanical properties of cancer cells and healthy cells as a single cell with a holographic imaging technique. The most important innovations brought by microfluidic chips are that they can perform many operations at the same time, cell separation processes, and the microchannels can be continuously identified and followed. They also provide a suitable environment for processing and analyzing cells in a narrow and restricted area. Therefore, the use of microfluidic chip applications in processes such as analysis, evaluation, replication on cells has become widespread. In the microfluidic systems developed within the scope of the thesis PDMS based microchips are produced and designed as a platform in which microchannels are contained, the cells can be immobilized individually and exposed to acoustic effects. HCT-116 (Colon Cancer), ONCO-DG-1 (Ovarian Cancer), MDA-MB-1 (Mammary Cancer) were chosen as the appropriate cancer

cell line and HUVECs (Human Umbilical Vein Endothelial Cells) selected as a healthy cell line for the experiments. First of all, a microfluidic system has been developed in which cells can be controlled. In order to control microfluidic systems, the flow must also be controlled. For this reason, a flow rate in the microfluidic system was measured by developing a micro-flow sensor based on diamagnetic levitation. Thanks to this developed sensor, optimum values were determined in the micro-flow system for cell culture studies. Afterward, ultrasonic transducers were integrated into the microfluidic system. Acoustic surface waves were created on cell surfaces using acoustic transducers. These transducers have been used to create discernible waves on the cell surface due to their high-frequency modes. As a result, the acoustic mechanical effect on cancer cells was obtained by the holographic imaging technique.

In experiments, acoustic waves were sent in the frequency range between 1 Hz and 2kHz and amplitude range between 3Vpp and 5Vpp applied to determine the mechanical stiffness of cancer cells. Optimum frequency ranges are determined, and results are compared. With these studies conducted in the thesis, a microfluidic system that can reveal the morphological structures of cancer cells based on acousto-holographic has been developed.

**Keywords:** Microfluidic, LoC (Lab-on-Chip), cancer, acoustic, holography

# ÖZET

## Tek Hücrelerin Mekanik Özelliklerinin Tespiti için Mikroakışkan Sistem Geliştirilmesi

Gizem AYDEMİR

Mekatronik Mühendisliği Bölümü

Master Tezi

Danışman: Dr.Öğr.Üyesi Hüseyin Üvet

Eş-Danışman: Prof. Dr. Ali Koşar

Bu tez kapsamında, holografik görüntüleme tekniğiyle tek bir hücre olarak kanser hücrelerinin ve sağlıklı hücrelerin mekanik özelliklerini belirlemek için mikroakışkan sistem geliştirilmiştir. Mikroakışkan çiplerin getirdiği en önemli yenilikler, aynı anda birçok işlemi gerçekleştirebilmeleri, hücre ayırma süreçleri ve mikrokanalların sürekli olarak tanımlanıp takip edilebilmeleridir. Ayrıca dar ve kısıtlı bir alanda hücreleri işlemek ve analiz etmek için uygun bir ortam sağlarlar. Bu nedenle, analiz, değerlendirme, hücreler üzerinde replikasyon gibi işlemlerde mikroakışkan çip uygulamalarının kullanımı yaygınlaşmıştır. Tez kapsamında geliştirilen mikroakışkan sistemlerde PDMS esaslı mikroçipler üretilir ve mikrokanalların bulunduğu bir platform olarak tasarlanır, hücreler ayrı ayrı hareketsiz hale getirilebilir ve akustik etkilere maruz kalabilir. Deneyler esnasında uygun kanser hücre hattı olarak HCT-116 (Kolon Kanseri), ONCO-DG-1

(Yumurtalık Kanseri), MDA-MB-1 (Meme Kanseri) ve sağlıklı bir hücre hattı olarak HUVEC'ler (İnsan Göbek Damarı Endotelyal Hücreleri) kullanıldı. Öncelikle, hücrelerin kontrol edilebildiği bir mikroakışkan sistem geliştirilmiştir. Mikroakışkan sistemleri kontrol etmek için de akışın kontrolü büyük önem taşımaktadır. Bu nedenle, mikroakışkan sistemdeki akış hızı diyamanyetik levitasyona dayalı bir mikro-akış sensörü geliştirilerek ölçülmüştür. Geliştirilen bu sensör sayesinde, mikrokültür sisteminde hücre kültürü çalışmaları için optimum değerler belirlenmiştir. Daha sonra, ultrasonik transdüserler mikroakışkan sisteme entegre edilmiştir. Akustik transdüserler kullanılarak hücre yüzeylerinde akustik yüzey dalgaları oluşturuldu. Bu akustik transdüserler, yüksek frekans modları nedeniyle hücre yüzeyinde fark edilebilir dalgalar oluşturmak için kullanılmıştır. Sonuç olarak, holografik görüntüleme tekniği ile kanser hücreleri üzerindeki akustik mekanik etki elde edildi.

Sonuç olarak, deneylerde, kanser hücrelerinin mekanik sertliğini belirlemek için 1 Hz ile 2 kHz frekans aralığında ve 3Vpp ile 5Vpp genlik aralığında akustik dalgalar gönderilmiştir. Optimum frekans aralıkları belirlenmiş ve sonuçlar karşılaştırılmıştır. Tezde yapılan bu çalışmalarla, kanser hücrelerinin morfolojik yapılarını akustik-holografik olarak ortaya çıkarabilen mikroakışkan bir sistem geliştirilmiştir.

**Anahtar Kelimeler:** Mikroakışkan, yonga üstü sistemler (Lab-on-Chip), kanser, akustik, holografi

# 1
# INTRODUCTION

## 1.1 Literature Review

Cancer is a leading cause of death worldwide, and tumor heterogeneity presents a challenge for the clinical management of the disease. The techniques used in determining the properties of cancer focus still contain some deficiencies. Traditional diagnostic methods require time-consuming, complex processes, and strict laboratory conditions. In classical approaches, it is widely used to consider and examine cells as a group to understand properties such as cell proliferation, differentiation, protein or gene expression, drug response, and toxicity experiments. However, examining the cell groups gives information about the average values. It is not a correct approach to make group analysis especially in heterogeneous diseases such as cancer. Due to the heterogeneous nature of cancer, individual examination of the morphological features of the single-cells is of great importance for drug trials [1-7].

Lab-on-chip systems scale down one or more laboratory functions on a single chip. This miniaturization has many advantages: it reduces costs by reducing the consumption of expensive reagents, the fluid flow is easy to control because the small dimensions often result in laminar flows, and the small dimensions also enable the handling of small particles like single cells.

The central aim of this thesis is to present a new microfluidic system for on-chip single-cell mechanical properties detection that can be applied to cancer diagnostics. The scope of this thesis is to develop a microfluidic system for single cancer cell mechanical properties detection.

## 1.2 Hypothesis of the Thesis

This thesis is the result of the project "A Holographic Single Cell Imaging Technique for Measuring the Mechanical Cell Stiffness of Circulating Tumor Cells using the Quantitative Phase Imaging Method". This Master project was funded by TUBITAK, in the framework of the "1003 program", which is a collaboration project between Yildiz Technical University, Marmara University, and Dokuz Eylul University. Also, this study was supported by the Scientific and Technological Research Council of Turkey (TUBITAK) with the scholarship through BİDEB 2210-C programme.

The thesis aims to develop a microfluidic system for three main applications. First, we developed microfluidic systems that would enable to cell culture on-chip, and a flow sensor has been developed for determining the parameters of the microfluidic system. Second, we create a comparative two dimensional and three-dimensional wound healing assay with wound generated via exclusively designed and magnetically manipulated micro-robot and the healing process is observed with a holographic imaging technique. Finally, Acoustic waves created on-chip for monitoring stiffness of living cancer cells.

## 1.3 Organization of Thesis

To understand the microfluidic system, we must begin with a discussion of how physical effects manifest at the microscale. In the first part of the thesis, we developed a microflow sensor prototype with zero mechanical contact in a microfluidic channel via diamagnetic levitation. Mathematical modeling, control, and experimental characterization of the micro-flow sensor is described. And then, we also describe the fabrication of microfluidic platforms for the detection of single-cell mechanical properties. The culturing of cancer cells to be used during the experiments and their integration into the microfluidic system are also described in this section. In Chapter 3, a Creation of Surface Acoustic Waves in A Microfluidic Device is constructed. In addition to the fabrication of the microfluidic device, parameters of the acoustic system are identified, based on experimental data. Then it is shown that that the design with the estimated

parameters can predict the behavior of the system very well. In Chapter 4, the acoustic test setup independent of the microfluidic system was established. Acoustic effects have been tested on the cell in different frequency ranges and optimum parameters have been determined. The acoustic system was then integrated into the microfluidic chip. Finally, the acoustic effect on the cells was tested with the holographic imaging technique and the results were compared.

# 2
# SENSOR DESIGN, FABRICATION, AND IMPLEMENTATION ON MICROFLUIDIC PLATFORM

## 2.1 Measurement of Flow Rate in Microfluidic System

Microfluidic systems have been heavily used in micro/nano robotics and biomedical applications. They play an important role in biomedical applications such as in vitro systems [1], thermal sensor systems [2-3], gas sensor systems [4-5], control and monitoring systems [6-7] and monitoring in vessel [8-9]. Micro robots, which are actuated via magnetic forces, are useful for many tasks such as cell manipulation [10-13], drug delivery [14-15], biopsy [16-17], and marking [18-19]. In a microfluidic environment, flow characteristics and environmental effects, related to acting forces on a microrobot change with decreasing dimensions. The reduction in the Reynolds number results in the formation of laminar flow condition. In laminar flow, the transfer and movement of micro objects become difficult. [20]. Therefore, it is important to measure the parameters of the fluid and flow. Moreover, Lab-on-a-chip technologies, which have gained significance during the last decade, are based on manipulating the flow in micro channels and actuation of particles/cells. Effective control of a microfluidic system is vital in this regard. Modeling the physical and mechanical properties of micro-systems is a major issue for efficiently designing microfluidic platforms. Measurements of parameters such as flow rate, viscosity and density are challenging in small scale.

In microfluidic systems, flow sensors are divided into two groups: thermal and non-thermal sensors. Thermal sensors function according to thermal transport principles. As an example, for thermal sensors, Glaninger et al. [21] fabricated a thermal sensor using a thin film germanium thermistor for a wide range of velocity measurements ($\pm 0.01$ to $\pm 200$) with a response time of less than 20 ms. The

major drawback of thermal flow sensors is the non-linearity of the calibration curve, which causes a sensitivity decrease in fluid flow rates [22]. Major system parameters are always dependent on the thermophysical properties, which affect sensor measurement parameters and hinders parallel and fast operation of microfluidic systems.

There are two approaches to achieve levitation: active and passive. The active levitation approach is used for systems using a feedback control loop, where passive levitation does not require any control. Passive magnetic levitation systems are impractical without any stabilizing component. Diamagnetic levitation can be used to add stability to passive levitation systems. Stability could be achieved without the need for a closed loop system.

Sensors based on levitation are useful for applications requiring precise results due to lack of mechanical contact. Diamagnetic levitation has been commonly implemented in many sensor studies. Velocity, displacement, force and accelerometer sensors using levitation have been recommended in the literature [23-26]. To achieve diamagnetic levitation, pyrolytic graphite is typically utilized. A feasibility study on diamagnetic levitation was first performed by William Thomson in 1847 [27]. Thereafter, diamagnetically stabilized levitation was applied by Boerdijk [28] for the first time. The Earnshaw Theorem states that external magneto static fields can be obtained using diamagnetic materials or super conductors [29]. Diamagnetic levitation using permanent magnets was discovered by Pelrine [30] as follows: Initially, a permanent magnet was levitated using a block of graphite, following the experimental path of the first superconductor levitation, and later it was discovered that the opposite was also possible [30].

As an example, for diamagnetic levitation studies, Hilber et al. [23] measured fluid density and viscosity in microfluidic systems with diamagnetic levitation, using a Hall Effect sensor. Such systems utilize magnetic coils for generating attractive forces. However, the magnetic coils might have complicated constructions, and in the micro scale, the driving current might lead to overheating problems.

In another study, Clara and co-workers [24] suggest that a diamagnetically levitated system can be treated as a spring-mass resonator. The resonance frequency of the setup depends on the levitation height of the floater magnet. It was also emphasized that the surrounding fluid has a damping effect on the fluid viscosity. However, the effect of flow rate on oscillations could not be determined. Under suitable conditions, diamagnetic materials allow to achieve stable levitation of permanent magnets in a passive fashion. Micro devices can achieve a submicron precision. The resulting mechanical friction might severely reduce the performance. Abadie and co-workers observed that a passive levitated seismic mass has spring oscillations in a nano force sensor design with diamagnetic levitation [25].

In this study, we proposed a sensor prototype with zero mechanical contact in a microfluidic channel via diamagnetic levitation. Since diamagnetic levitation is used, the lateral forces of the micro-magnet in the channel are rather low. Thanks to the advantage of diamagnetic levitation, the smallest displacements on the X-axis can be easily detected when the micro-magnet motion within the channel is achieved. The developed sensor has a stable system, which can detect low flow rates. Levitation was accomplished with pyrolytic graphite and a ring magnet (NdFeB) configured as a “lifter-magnet”. The displacement of the micro-magnet in the micro channel in longitudinal direction was monitored via a microscope-camera system and was measured via a laser sensor above the lifter-magnet. Precise measurement is achieved by using this method. The proposed sensor methodology can sense flow rates as low as 1000 µl/min. The uncertainty in the flow rate is ± 3.6%. The suggested system can be well integrated to microfluidic systems. While the corresponding Reynolds number is between 5.4 and 37.9 for the system, the measured flow rate range was varied between 1000 µl/min and 7000 µl/min. This sensor is applicable for the systems to be used in micro robotics applications, monitoring in vessel, respiratory monitoring, monitoring capillary microcirculation and biomedical applications.

### 2.1.1 System Methodology

The sensor system houses the magnetic levitation setup, pyrolytic graphite in an acrylic container and the channel configuration (as shown in Fig.1). Pyrolytic graphite is a diamagnetic material, and a low magnetic force is exerted on diamagnetic materials when they are in the proximity of a permanent magnet. The atoms of diamagnetic materials do not have any constant magnetic dipole moment. However, it is possible to generate magnetic dipole moment with the effect of outer magnetic field. The direction of the magnetic moment is in the opposite direction compared to the magnetic field. This approach allows diamagnetic materials to apply a repulsive force on permanent magnets, which facilitates the levitation.

The NdFeB (neodymium) ring magnet functions as a lifter-magnet in the system connected to the micro stage. Micro flows with flow rates between 1000 $\mu$l/min and 7000 $\mu$l/min are generated in the channel via a syringe pump (Cole Parmer). Deionized water is used as the working fluid. X-Z axis displacement of the magnet is measured with a laser sensor (Micro-Scanner). Laser sensor is used for closed-loop control of the position of the magnet in the channel. It provides stable and precise position measurements. The resolution of the laser sensor used in the X-axis is 1280 points/profile, and the reference resolution in the Z-axis is 2 $\mu$m. The experimental data points are acquired, while the sensor profile frequency is 100 Hz. The microscope-camera lens system (Olympus SZX-7 and Point Grey GS3-U3) is vertically positioned on the side profile to allow for the observation of the movement of the micro-magnet in the channel, as well as levitation. The movement of the micro-magnet in X-Z axis while levitation is controlled via an interface designed with Visual Studio – C#.

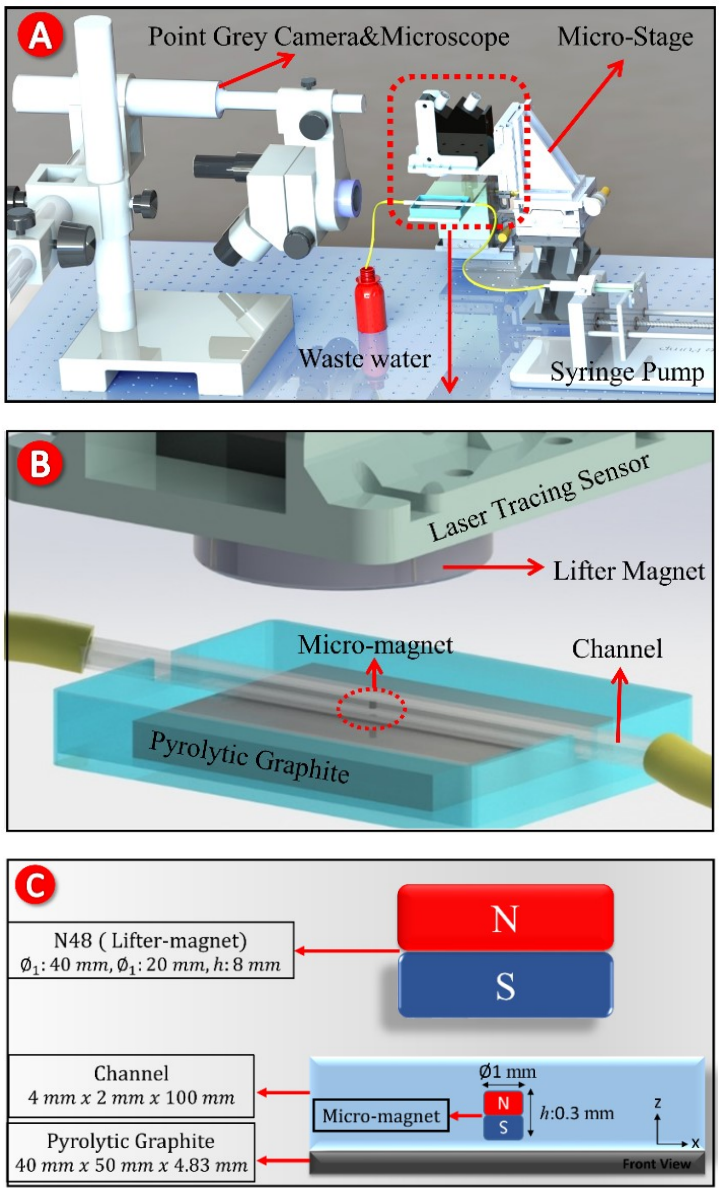


**Figure 2.1** The experimental setup: Flow rate in the micro channel is measured with diamagnetic levitation utilizing laser tracking. The magnets are made of NdFeB with remanence magnetic field strength of 1.37 T for a volume of $1cm^3$. The air gap between ring magnet and micro-magnet is 50-51 mm.

### 2.1.2 Theory and Data Reduction

The free body diagram for the micro-magnet in the channel on Z-axis is given in Figure 2.2. The glass channel is placed on pyrolytic graphite, which is in an acrylic container. The displacements of diamagnetically levitated (via lifter-magnet) magnet corresponding to flow rates of between 1000 $\mu$l/min and 7000 $\mu$l/min are

detected with a laser sensor. The major parameters are included in Table 2.1 The levitation is along the Z-axis, while the movement is along the X-axis.

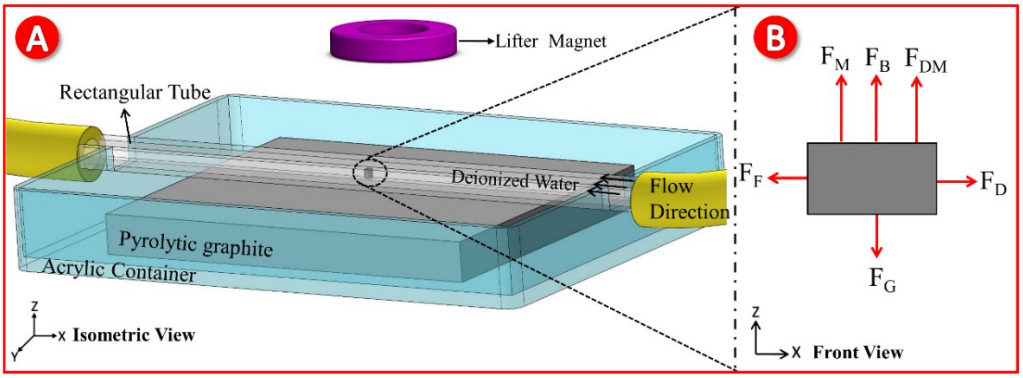


**Figure 2.2** Fig.2.2A Concept of the flow sensor. Fig.2.2B Free body diagram for the micro-magnet in lateral and vertical directions. Magnetization of the magnets is in the Z axis. Magnetic and diamagnetic forces are calculated along the Z axis. In order to achieve levitation, the buoyancy force, diamagnetic force applied by pyrolytic graphite and attraction force of the lifter-magnet must be equal to the weight of the micro-magnet.

**Table 2.1** Major parameters of the sensor.

| Symbol | Parameter | Unit |
|---|---|---|
| $F_B$ | Buoyancy Force | N |
| $F_D$ | Drag Force | N |
| $F_{DM}$ | Diamagnetic Force | N |
| $F_G$ | Gravitational force | N |
| $F_F$ | Flow Force | N |
| $F_M$ | Magnetic Force | N |
| A | Cross-Sectional Area | $m^2$ |
| $\mu_r$ | Magnetic Permeability of Space | |

**Table 2.1** Major parameters of the sensor. (Cont.)

| | | |
|---|---|---|
| $\mu_0$ | Magnetic Conductivity Number | Wb/Am |
| H | Magnetic Field | A/m |
| $M_{dia}$ | Magnetization Vector | A/m |
| $\chi$ | Magnetic Susceptibility Factor | - |
| B | Magnetic Flux Density | T |

The continuity equation for incompressible flows along the channel is expressed as:

$$\nabla . u = 0 \tag{2.1}$$

The Reynolds Number is defined as [31]:

$$R_e = \frac{\rho . v . D_h}{\mu} \tag{2.2}$$

Reynolds Number is between 5.4 and 37.9 corresponding to flow rates between 1000 $\mu$l/min and 7000 $\mu$l/min. Thus, the flow is laminar.

The momentum equation is given as [32]:

$$\rho \frac{\partial \vec{v}}{\partial t} = -\vec{\nabla} P + \rho \vec{g} + \eta \nabla^2 \vec{v} + \overrightarrow{F_M} \tag{2.3}$$

Here, $v$ is flow velocity, $\rho$ is density, $\mu$ is viscosity and $p$ is pressure. The force is applied by the lifter-magnet on the micro-magnet in the channel and affects a small volume *(dV)* of the magnet is experessed as:

$$d\vec{F} = \mu_0 \nabla (\vec{M} . \vec{H}) \tag{2.4}$$

Here $M$ is the magnet's magnetization, $H$ is the magnetic field strength. The total force on magnet can be found as:

$$\overrightarrow{F_m} = \int_V \; d\vec{F} dV \tag{2.5}$$

The forces in cylindirical coordinates are as follows:

$$\overrightarrow{F_z} = \int_V d\overrightarrow{F_z} - \mu_0 \int_V \frac{\partial}{\partial z}(M_0 H_z) \text{ (Z axis)} \quad (2.6)$$

$$\overrightarrow{F_x} = \int_V d\overrightarrow{F_x} - \mu_0 \int_V \frac{\partial}{\partial x}(M_0 H_z) \text{ (X axis)} \quad (2.7)$$

$$\overrightarrow{F_y} = \int_V d\overrightarrow{F_y} - \mu_0 \int_V \frac{\partial}{\partial y}(M_0 H_z) \text{ (Y axis)} \quad (2.8)$$

For the calculation of the diamagnetic force, the uniform medium assumption is made. Accordingly, this force is stated as:

$$d\boldsymbol{F} = M_{dia}(\nabla \boldsymbol{B})dV \quad (2.9)$$

The diamagnetic force between pyrolytic graphite and the magnet can be written as [33]:

$$F_{dia,x} = \frac{X_{dia}}{2\mu_0} \iiint_V \left(\frac{\partial \|B\|^2}{\partial x}\right) dV \quad (2.10)$$

$$F_{dia,y} = \frac{X_{dia}}{2\mu_0} \iiint_V \left(\frac{\partial \|B\|^2}{\partial y}\right) dV \quad (2.11)$$

$$F_{dia,z} = \frac{X_{dia}}{2\mu_0} \iiint_V \left(\frac{\partial \|B\|^2}{\partial z}\right) dV \quad (2.12)$$

According to the above expression, for a pyrolytic graphite with dimensions of $40x50x4.83\ mm$, this force is calculated as 3.75 μN [34].

The expressions of gravitational force, buoyancy force and drag force are given as:

$$F_G = m_m g \quad (2.13)$$

$$F_B = V_m \rho_f g \quad (2.14)$$

$$F_D = \frac{1}{2} c_d \rho_f A v^2 \quad (2.15)$$

Here, $m_m$ is mass of micro-magnet, $V_m$ is volume of micro-magnet, $\rho_f$ is density of fluid.

The drag force is a function of the fluid velocity and density along with the object's reference area and drag coefficient $C_d$.

The $C_d$ coefficient equation is stated as [35]:

$$C_d = \frac{24}{Re}\left(1 + \frac{Re^{2/3}}{6}\right)$$

The forces exerted on the micro sensor are shown in Fig.2.2. For a micro-magnet in the channel with a mass of 2.72 $\mu$g, the micro-magnet displacement can be determined for known values of buoyancy force, magnetic force, diamagnetic force and gravitational force.

The micro-magnet buoyancy force in the flow channel is calculated as 2.36 $\mu$N. The average drag force applied on the system is estimated of 6.52 $\mu$N when the flow rate is between 1000 $\mu$L/min and 7000 $\mu$L/min. The micro-magnet gravity force in the channel is calculated as 26.68 $\mu$N. The magnetic force applied on micro-magnet in the channel is thus between 14.52 $\mu$N and 15.37 $\mu$N in the light of analysis.

**Table 2.2** Major parameters of the sensor

| Symbol | Parameter | Quantity |
|---|---|---|
| $F_B$ | Buoyancy Force | 2.36 $\mu$N |
| $F_D$ | Drag Force | 6.52 $\mu$N |
| $F_{DM}$ | Diamagnetic Force | 3.75 $\mu$N |
| $F_G$ | Gravitational force | 26.68 $\mu$N |
| $F_M$ | Magnetic Force | 14.52-15.37 $\mu$N |
| Re | Reynolds Number | 5.4-37.9 |

The values obtained from the analysis can provide force balance in the system. Since the force balance is accomplished, the micro-magnet inside the channel is stationary in the vertical direction.

In micro systems, vibrations have a considerable impact. Therefore, they constitute an important issue. An active zero-power controlled magnetic

suspension system was suggested in the literature to control vibrations [36]. Vibrations in a system might cause serious deformation and are often observed in magnetic levitation systems. Resonance frequency is related to the dimensions and mass of the object. When the systems are massive, the vibrations can be compensated. However, in micro scale, vibrations become more problematic because smaller objects tend to oscillate much more than relatively larger objects. Electrostatic forces are more dominant in micro-scale systems compared to gravitational forces. Eddy current damping is the optimum method of adding extra damping to levitation systems because of its non-contact nature. Eddy current dampening has been used to suppress ambient vibrations [37]. Similar to the results of Morita *et* al. [38] it was observed that magnetic levitation suffers from vibrations due to contactless motion and low environment stiffness. In addition, it was observed that undesired vibrations increase in magnetic levitation, as the object size becomes smaller.

The micro-magnet in a channel under magnetic field can be modeled with a spring-mass-damper system for given flow rates. The forces applied on the object are acquired from the analysis results and are utilized as an input for the spring-mass-damper model. In the numerical model, the magnet makes an angle with the lifter-magnet (Fig.2.3). During simulations, this angle $\theta$ changes due to the magnet's position relative to the lifter-magnet. Harmonic oscillations occur with a change in the angle. In our system, the resonance frequency of the sensor was measured by experiments. Vibrations were observed in the micro-magnet during experiments. Accordingly, the displacement of the micro-magnet was measured by the laser sensor. Due to the precision of the laser sensor (a resolution of 2 $\mu$m), 155 data points were acquired and processed for each measurement. Using these data points, the frequency of the system was measured for flow rates between 1000 $\mu$l/min and 7000 $\mu$l/min. According to the results, the system resonance frequency was found as 12.8 Hz for the flow rates between 3000 $\mu$L/min and 3500 $\mu$L/min.

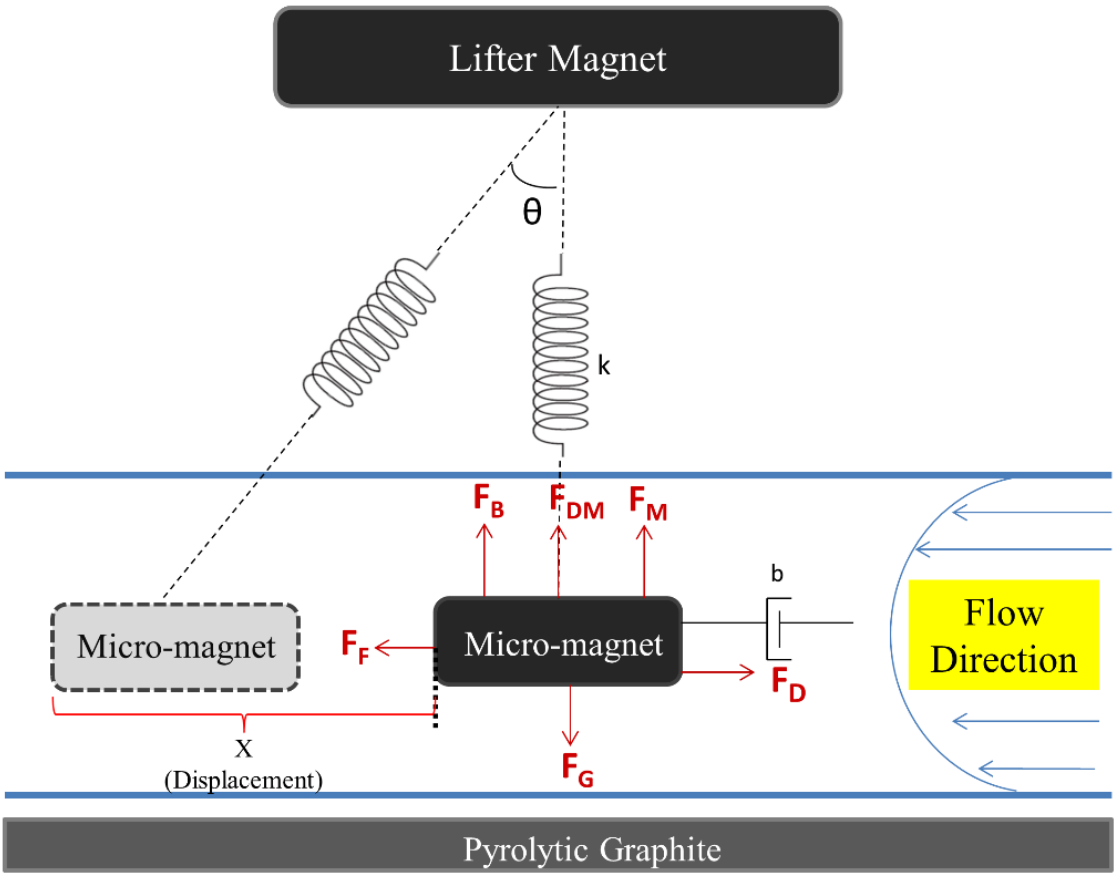


**Figure 2.3** Modelling of micro-magnet in the channel as a spring-mass-damper system.

Considering that a single frequency sinusoidal vibration is applied to the system, the general equation of motion is given as:

$$F_0 cos(\omega t) = m.\ddot{x} + c.\dot{x} + kx \tag{2.16}$$

where $m$ is the mass of micro-magnet, $x$ is the displacement of the micro-magnet, $c$ is the damping coefficient, $k$ is the stiffness coefficient, $F_0$ is the maximum amplitude of the disturbance, ω is the frequency of vibration, and $t$ is time. The resonant frequency is expressed as:

$$\omega_0 = \sqrt{k/m} \tag{2.17}$$

Figure 2.4 shows frequency and amplitude plots for flow rate is between 1000 $\mu$L/min and 4500 $\mu$L/min based on the experimental results. As seen in Fig 2.4, when the flow rate is increased, frequencies for flow rates between 1000 $\mu$l/min

and 2500 $\mu$l/min, 3000 $\mu$l/min and 3500 $\mu$l/min are 10 Hz, 11.12 Hz and 12.14 Hz, respectively.

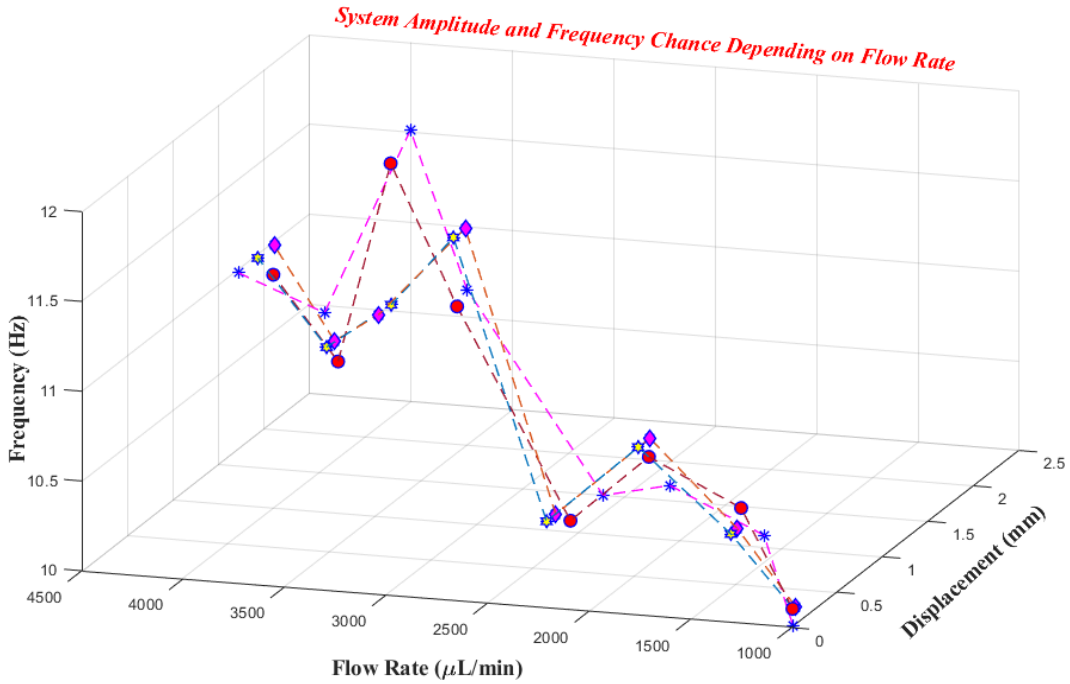


**Figure 2.4** Vibration frequency of the system between 1000 $\mu$l/min and 5000 $\mu$l/min. Displacements represent amplitudes of the system. The system shows visible harmonic oscillations for flow rates 3000 $\mu$l/min and 3500 $\mu$l/min.

### 2.1.3 Simulations

The simulations are performed using the software COMSOL Multiphysics Version 5.3 (CPU License No: 17076072). For generating the 3D mesh structure, extra fine free tetrahedral mesh elements with 354.037 elements were used. A typical mesh is shown in Fig.2.5. A workstation with an Intel Xeon 3.50 GHz processor with 32 GB RAM was utilized for this task. The server's operating system was Windows-10 64-bit edition.

Flow and magnetic field analyses were performed for the sensor system. AC/DC module of the software COMSOL Multiphysics Version 5.3 (CPU License No: 17076072) is implemented for assessing the effect of magnetic field on the object. The reason for performing magnetic analysis is to estimate the magnetic forces

and to find the distance between micro-magnet and lifter-magnet. Fig. 2.6 shows the mesh structure.

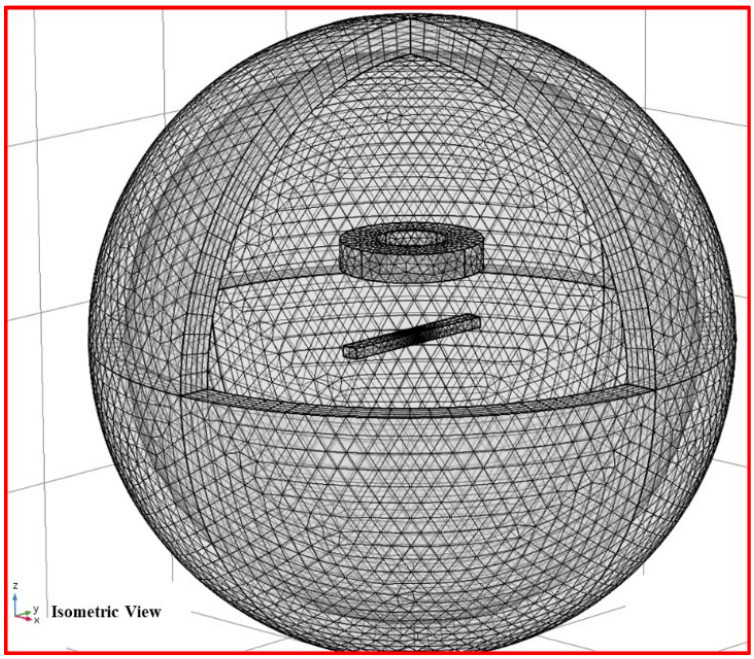


**Figure 2.5.** The mesh structure of the system. Fine, finer and extra fine meshes are used. Grid independency is achieved.

The magnetic flux density is calculated by dynamic analysis depending on the movement of the micro-magnet in the channel. Figure 2.6 shows magnetic flux density between the lifter-magnet and micro-magnet in the channel. The magnetic flux density is obtained in 0.5 mm increments from 0 mm to 3.5 mm depending on the displacement of micro-magnet. As the directions of magnetization on the lifter-magnet and micro-magnet are in Z-axis, magnetic field lines are also in the same directions.

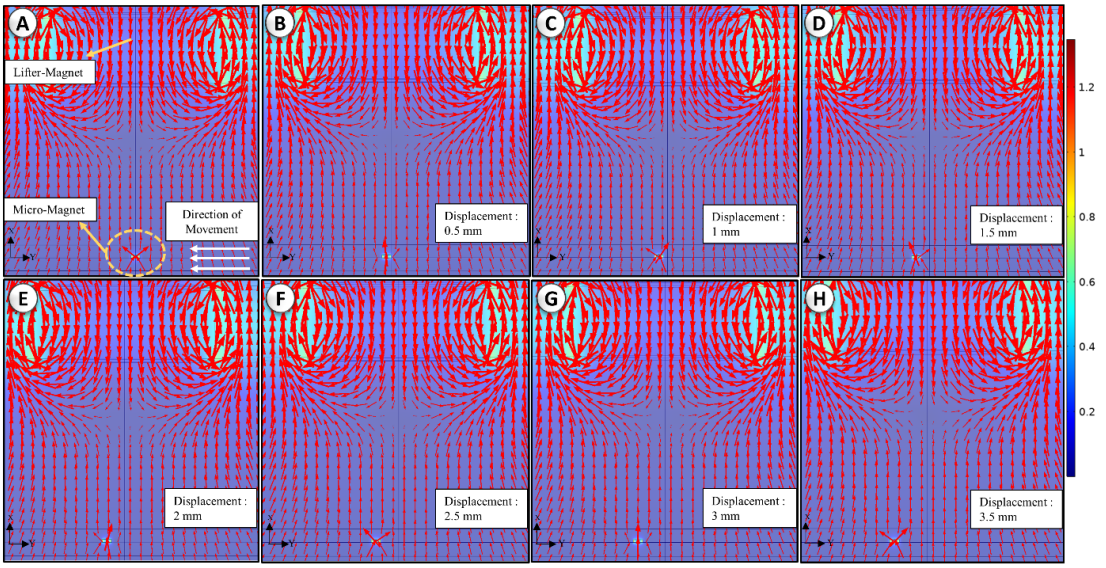


**Figure 2.6** Magnetic flux density between the lifter-magnet and micro-magnet in the channel. Remanent flux density of the magnets is chosen as 1.3 T in the light of material properties. Magnetization of the magnets is on the horizontal axis.

Magnetic force acting on the micro-magnet in the Y-axis is calculated and is displayed in Figure 2.7.

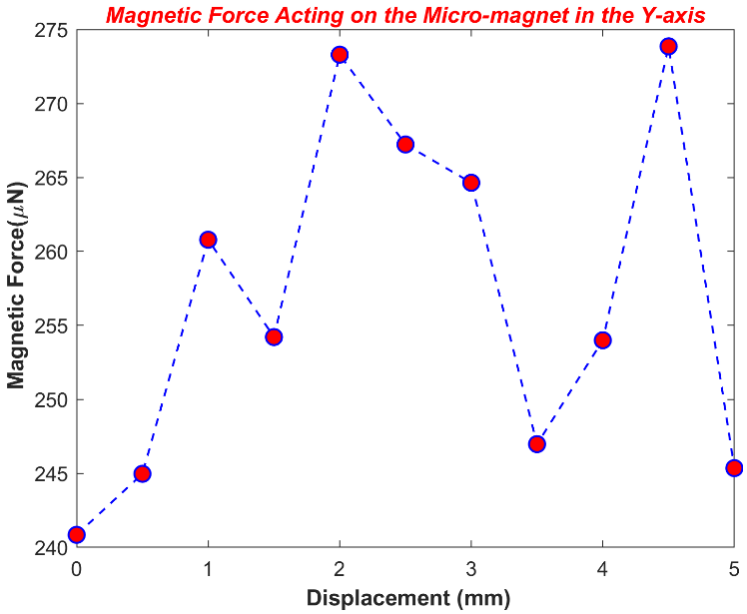


**Figure 2.7** Vertical magnetic force acting on the micro-magnet as a function of the displacement when micro-magnet moves with the flow.

**Table 2.3** Dimensionless susceptibility χ in SI units for some diamagnetic materials [40].

| **Material** | $-\chi(\mathbf{10^{-6}})$ |
|---|---|
| Water | 8.8 |
| Gold | 34 |
| Bismuth Metal | 170 |
| Graphite Rod | 160 |
| Pyrolytic Graphite ∟ | 450 |
| Pyrolytic Graphite ‖ | 85 |

Table 2.3 shows dimensionless susceptibilities of some diamagnetic materials [40]. As seen, pyrolytic graphite has the highest dimensionless susceptibility($450x10^{-6}$). The magnetic flux density for the distance between micro-magnet and lifter-magnet of 50 mm (when micro-magnet is levitated) is shown in Fig.2.8. The distance between the micro-magnet and the lifter-magnet was found via this magnetic analysis. The magnetic force applied on the micro-magnet in the channel is determined as a function of the distance between the micro-magnet and lifter-magnet. The distance between the lifter-magnet and micro-magnet is increased from 10 mm to 60 mm, and the magnetic forces acting on the micro-magnet in the channel are obtained over this distance range. Accordingly, the micro-magnet in the channel can be levitated when the distance between the lifter-magnet and micro-magnet is 50-51 mm. The magnetic force on the micro-magnet establishes the balance of forces generated in the mathematical model.

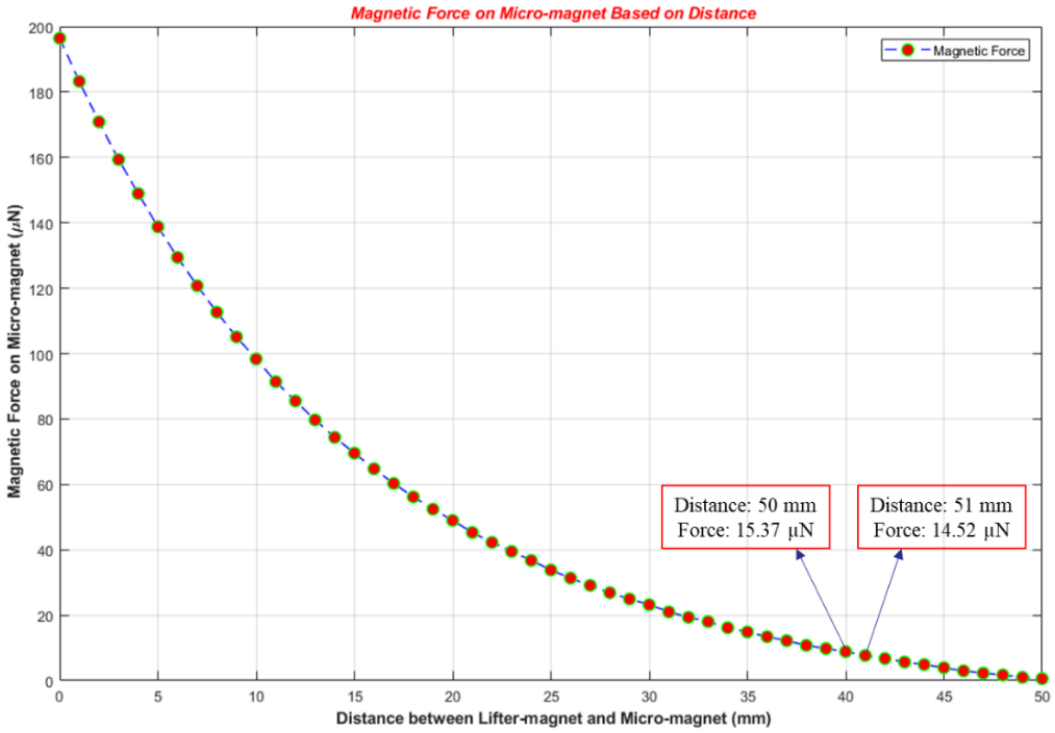


**Figure 2.8** Magnetic force acting on micro-magnet as a function of the distance between the micro-magnet and lifter-magnet. The micro-magnet in the channel remains stationary while lifter-magnet attached to the micro-stage is moved away from it. Magnetic force decreases when the lifter-magnet is moved further away.

As shown in Fig. 2.8, as the distance between the micro-magnet and lifter-magnet is increased, the force applied on the micro-magnet decreases.

The distance between the lifter-magnet and the micro magnet in the channel was determined using AC/DC module of the software COMSOL. However, the micro-magnet in the channel moves depending on the flow. Regarding Fig. 2.9 and 2.10, magnetic force varies when the micro-magnet moves along the microchannel. Also, the micro-magnet vibrates in the Z-axis when it moves. Since diamagnetic stability plays an important role in the application of the passive micro-flow sensor, the Z-axis stability analysis was performed. Diamagnetic stabilized magnetic levitation have been recommended in the literature [40]. In this study, different configurations and conditions for diamagnetic stability were described.

The potential enegy of a micro-magnet with magnetic moment $\vec{M}$ (magnitude $M$) in the range of affect of a lifter-magnet with the magnetic flux density $\vec{B}$ (magnitude $B$) is

$$U = -\vec{M}\,\vec{B} + mgz = -MB + mgz \tag{2.18}$$

where $mgz$ is the gravitational energy with mass $m$ of the micro-magnet, gravitational acceleration $g$, and the distance of the micro-magnet ortogonal to earth surface $z$. Due to the magnetic torques, the micro-magnet is aligned in the direction of the local field, so the energy varies only with the magnitude of the magnetic field.

For the stability condition in the Z-axis of the micro-magnet, the magnitude of the lifter-magnet magnetic flux density was expanded around the levitation point (z= 0) in polar coordinates. The terms $C_r r^2$and $C_z z^2$ representing the effect of the diamagnetic material have been added. $C_r r^2$shows the horizontal effect and $C_z z^2$shows the effect vertically. The potential energy of the micro-magnet in this case is

$$U = -M\left[B_0 + \left\{B' - \frac{mg}{M}\right\}z + \frac{1}{2}B''z^2 + \frac{1}{4}\left\{\frac{B'^2}{2B_0} - B''\right\}r^2 + \cdots\right] + C_z z^2 C_r r^2 \tag{2.19}$$

where

$$B'\frac{\partial B_z}{\partial z} \quad \text{and } B''\frac{\partial^2 B_z}{\partial z^2} \tag{2.20}$$

The total force on the Z-axis at the levitation point must be zero. Therefore, equation 19 is expressed as follows;

$$B'\frac{mg}{M} \tag{2.21}$$

The conditions for vertical stability is

$$K_v \equiv C_z - \frac{1}{2}MB'' > 0 \tag{2.22}$$

As stated in equation 22, when $K_v > 0$, levitation is vertically stable.

In the study of Simon et al. [40] for the calculation of $C_z$, five different methods are stated. The following equation is used in the calculation of $C_z$

$$C_Z\frac{6M^2|\chi|\mu_0}{\pi D^5} \tag{2.23}$$

Stability analysis has been performed to determine the 'stable levitation' points, which is shown in Fig.2.9. While the distance between the lifter magnet and the micro-magnet is between 50 mm and 51 mm, it shows stable and unstable points when micro-magnet moves in the channel.

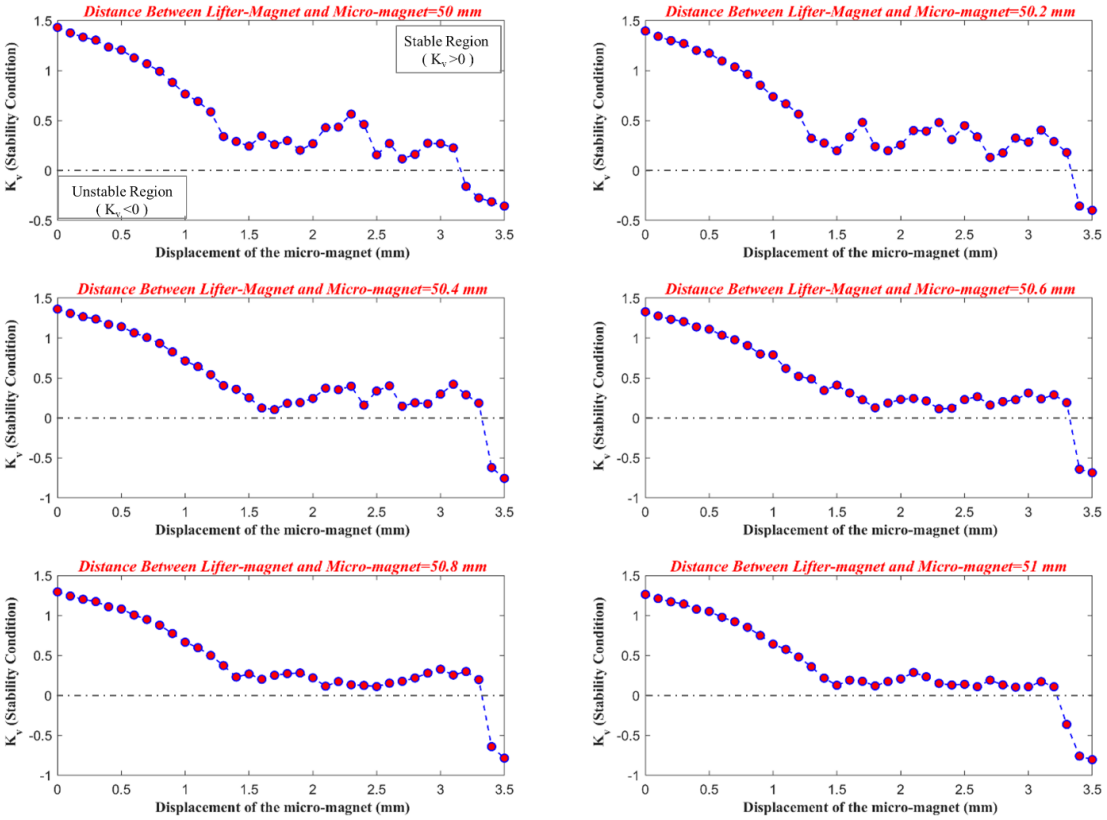


**Figure 2.9**. Stability functions $K_v$ for ring magnet with outer dimension 40 mm and inner dimension 20 mm. The X-axis is displacement of the micro-magnet in the channel. Levitation is stable where $K_v$ is positive.

As can be seen from Figure 2.9, the micro-magnet in the channel is in the stable region when it moves in the range between 0 mm and 3 mm with 0.1 mm intervals. When the micro-magnet moves more than 3.3 mm, it becomes unstable.

The Flow Module of the software COMSOL Multiphysics Version 5.3 (CPU License No: 17076072) is used for modelling flows. The Laminar Flow interface is used to obtain the velocity and pressure fields for flows of a single-phase fluid in the laminar flow regime (Fig.2.11). Governing equations (Navier Stokes equations

and continuity equation) are solved via the Laminar Flow interface. The forces acting on the micro-magnet in the channel are calculated. Flow rates between 1000 $\mu$L/min and 6000 $\mu$L/min are considered as an input. Fig.2.11 shows that the micro-magnet suddenly accelerates at 5000 $\mu$L/min. This sudden acceleration is also observed in the experimental results at 5000 $\mu$L/min. When generating the flow model, the ALE (Arbitary Lagrangian-Eulerian) approach is taken as the numerical scheme.

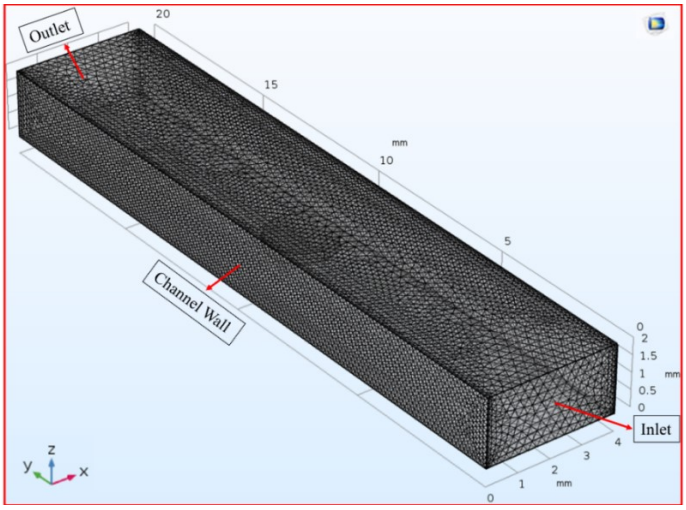


**Figure 2.10**. The mesh structure. The flow was modeled using single-phase and incompressible flow assumptions via the Laminar Flow Module interface. No slip velocity boundary condition on the walls, flow rates of between 1000 $\mu$l/min and 7000 $\mu$l/min at the 'Inlet' and atmospheric pressure on the surface at the 'Outlet' were imposed as the boundary conditions.

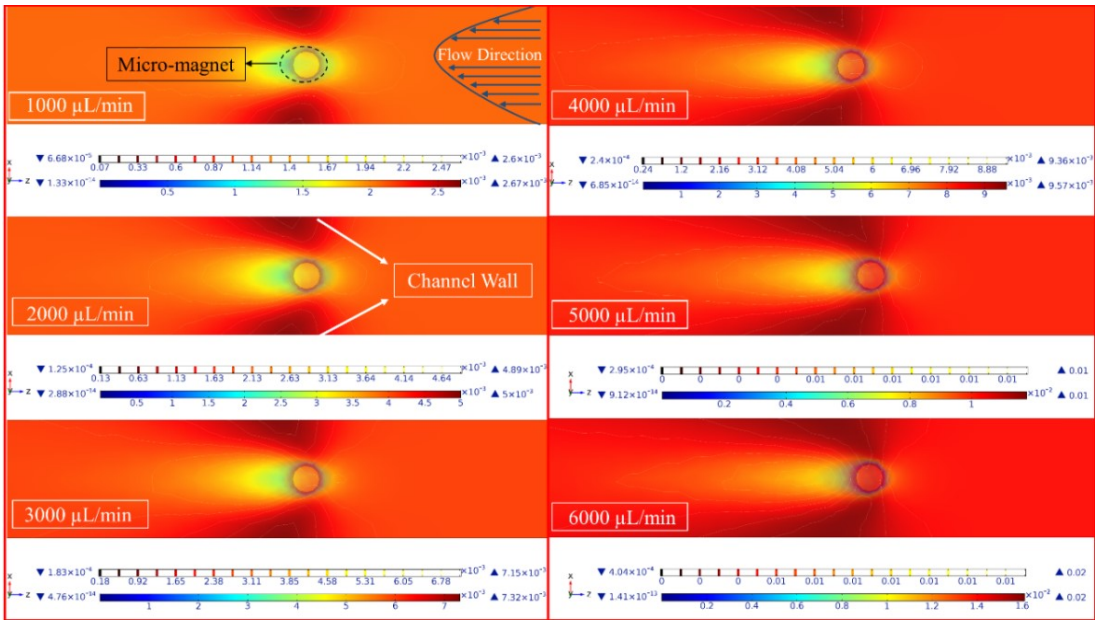


**Figure 2.11** Flow force acting on the micro-magnet for flow rates between 1000 $\mu$L/min and 5000 $\mu$L/min. Flow rates between 1000 $\mu$L/min and 6000 $\mu$L/min are inputs for the analysis.

The effect of the flow acting on the micro-magnet as a result of the flow analysis was determined. Thus, movement of magnet in the channel occurs as a result of interaction between the micro flow area and the magnetic field.

### 2.1.4 Experimental Results

Figure 2.12 shows the captured images using the Point Grey microscope camera during the experiments. During the experiments, the micro-magnet moves between 0.0016 and 3.28 mm in the channel depending on the measured flow rate. Displacements of 0.0016-1.5 mm are measured for a flow rate range of between 1000 µL/min and 3000 µL/min, while the displacements for the range of between 3000 µL/min and 5000 µL/min flow rates are between 1.5 mm and 2.25 mm. At flow rates above 7000 µL/min, the levitation of the micro-magnet deteriorates, which implies that the proposed sensor can measure flow rates up to 7000 µL/min.

Fig. 2.13D and Fig.2.13E show the deterioration in levitation, where the micro-magnet occasionally deposits to the bottom of the channel and sometimes sticks to the top boundary of the channel. When the levitation height is bigger than 200

$\mu$m (the distance between the micro-magnet and the lifter-magnet is 51 mm), the magnetic force dominates over the gravitational force, which makes the micro-magnet stick to the top of the channel. Similarly, if the levitation height is smaller than 140 $\mu$m, the gravitational force is greater than the magnetic force, then the micro-magnet deposits to the bottom of the channel.

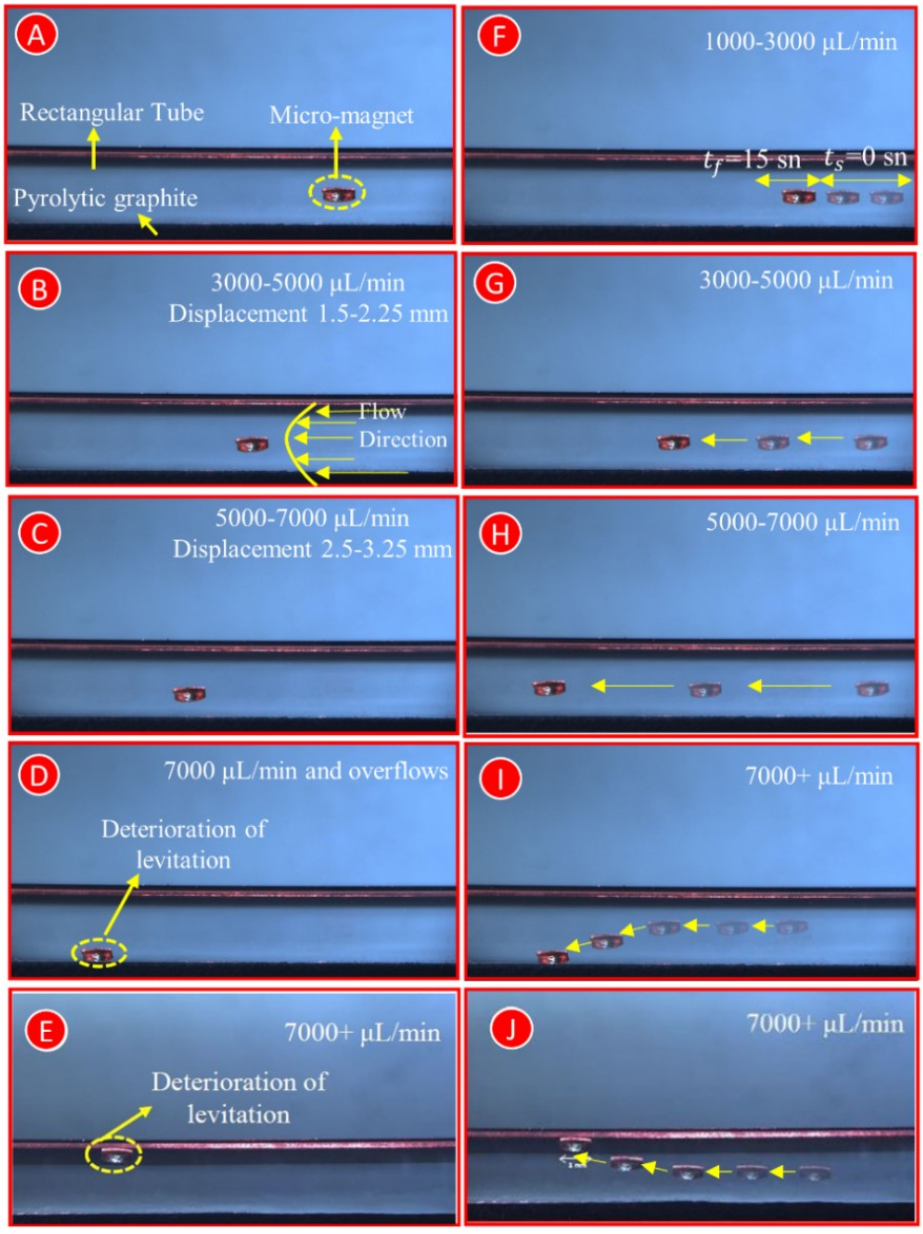


**Figure 2.12.** Images captured from the Point Grey microscope camera system during the experiments. Figures A-B-C-D-E display the amount of displacement depending on the flow rate. F-G-H-I-J show the applied flux-dependent and time dependent behavior of the magnet.

The levitation heights change in contrast to the distance between the micro-magnet and lifter-magnet, which is fixed in the experiments. Displacements for flow rates between 1000 $\mu$L/min and 7000 $\mu$L/min at 7 different levitation heights are shown in Figure 2.13.

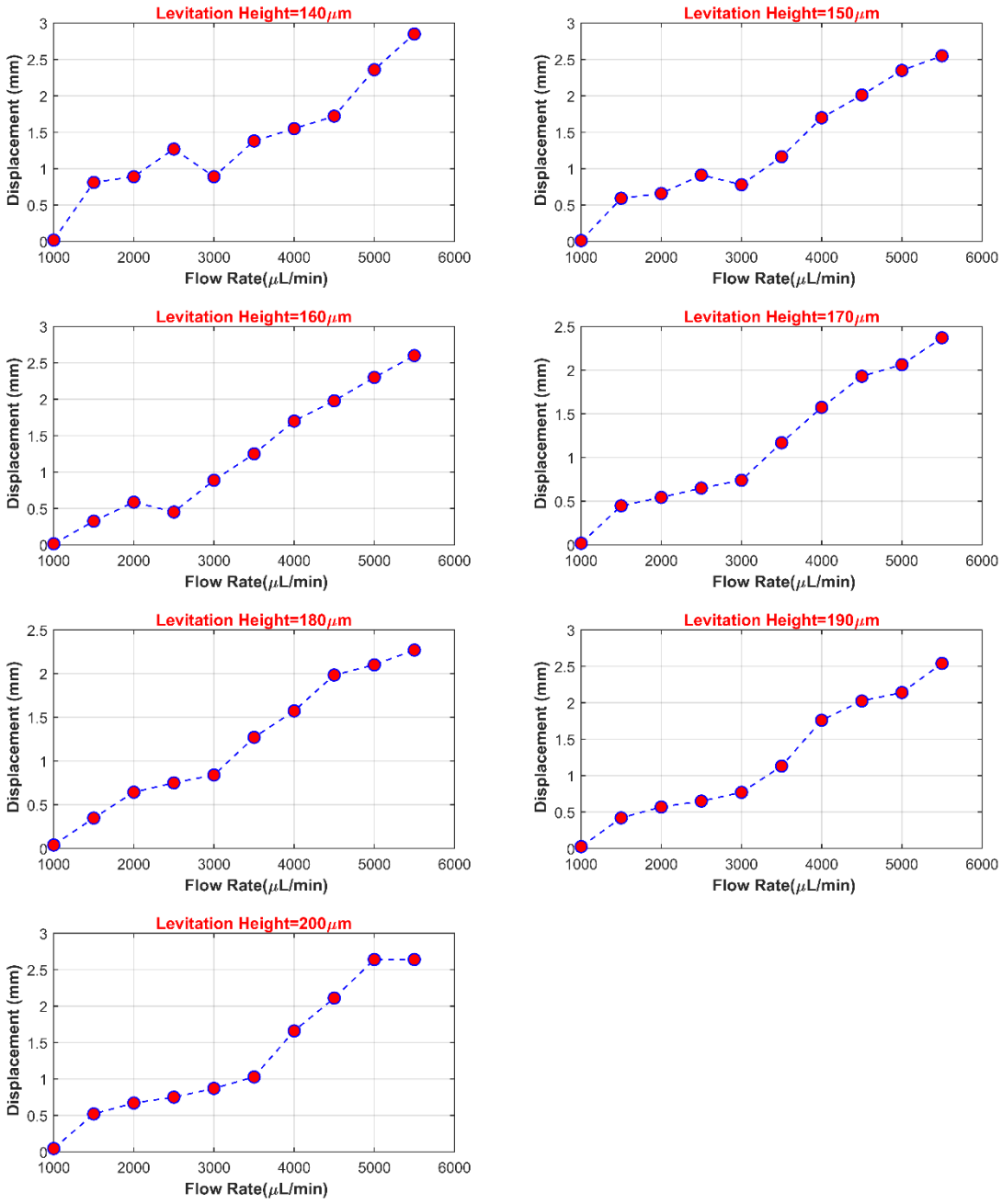


**Figure 2.13**. Different levitation heights of 7 experiments, the displacements at the flow rates between 1000 µL/min and 7000 µL/min were investigated.

As seen in the related figures (Fig.2.13. and Fig.2.14), the levitation heights do not affect the results because P>0.05 according to the t-test. Fig.2.13 shows the

behavior of the magnet at these levitation heights. The p-test was used to compare the groups at different levitation heights of the micro-magnet. This comparison result shows that the micro-magnet has a levitation height between 140 $\mu$m and 200 $\mu$m, while it does not alter the measurement of the sensor from this levitation height range.

The data points were required at different levitation heights with 10 $\mu$m intervals. Student t-test was performed for the last 7 experimental data. The comparison of average and standard deviation amongst last seven experiments corresponding to different levitation heights (56 sets of each experiment) is shown in Fig.2.14. Moreover, each experiment was repeated for 20 times to check for the repeatability.

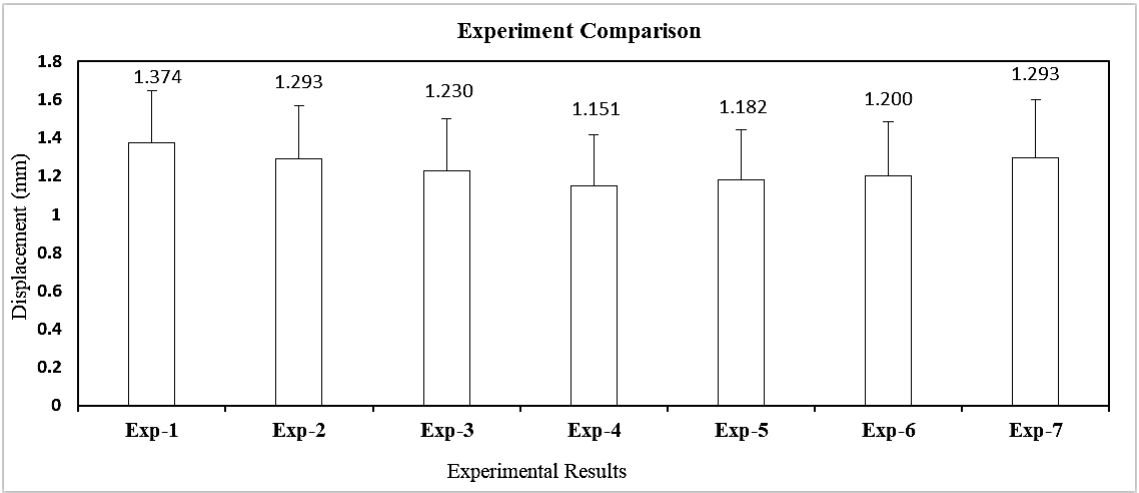


**Figure 2.14.** Comparison of average and standard deviation amongst last seven experiments corresponding to different levitation heights (56 sets of data).

Curve fitting based on the Least Squares method is performed to correlate the flow rate with the displacement. Accordingly, correlation coefficient ($R^2$) of 0.938 is obtained. Thus, the flow rate can be expressed in terms of the following calibration curve (Fig.2.15):

$$Flow\ Rate\left[\frac{\mu L}{min}\right] = 1658x + 1054\ [mm]\ , \qquad x\text{: } displacement\ (mm)$$

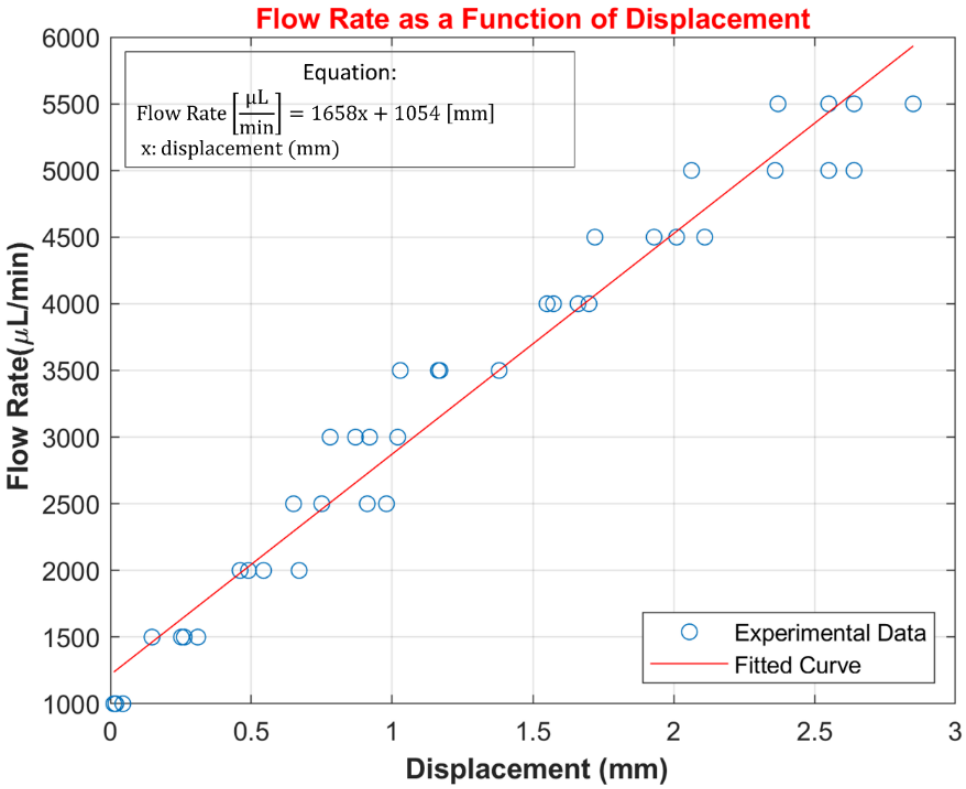


**Figure 2.15**. Obtained calibration curve

This study presents a passive micro flow sensor based on diamagnetic levitation. Flow rates between 1000 $\mu$L/min and 7000$\mu$L/min can be measured in microfluidic devices with this sensor. Levitation was accomplished with by pyrolytic graphite and a ring magnet (NdFeB) acting as a lifter. The displacement of the micro-magnet in the micro channel in longitudinal direction was monitored via a microscope-camera system and was measured via a laser sensor above the lifter-magnet. The uncertainty in flow rate measurement is ±3.6% based on the used equipment. Modeling and analysis of the system are performed and are accompanied with the experiments. This sensor is applicable for the systems to be used in micro robotics applications, monitoring in vessels, respiratory monitoring, monitoring capillary microcirculation and biomedical applications. The presented sensor is compact, does not require any external power, allows for parallel and faster processing to have higher throughput, and is easily integrable to other systems. In the future, it is aimed to realize viscosity and density measurements as well as to integrate the sensor to lab-on-a-chip applications.

## 2.2 Microfluidic Chip and Micro-robot Fabrication

The microfluidic chip produced within the scope of the thesis is designed as a platform in which microchannels are located and the cells are individually immobilized. Microfluidic chip production was carried out under clean room conditions and using UV lithography technique. In addition to this method, microfluidic chips were produced using PMMA (Polymethyl methacrylate) and DSA (Double-sided tape) materials. The two methods have their advantages and disadvantages. Nano-sized microchannel can be achieved in the microfluidic chip by UV lithography. (In this context, PMMA and DSA and microfluidic channels have been produced to display the cells and find the optimum acoustic frequency. It has optical transparency (between 450nm-700nm wavelengths), it can be used in applications such as laser CNC and hot cutting, it is an organic sub-based material, The compatibility between the cells and the low cost is the main advantage of the PMMA material. The disadvantage of this method is that the laser cutting device has poor tolerances and a minimum of 500 $\mu$m wide and 1.5 mm high microfluidic channels can be produced. Experiments have been carried out with microfluidic chips produced by lithography at the stage. Methods and steps used in the production of microfluidic chips:

1. By using lithography technique in clean room standards
2. Using PMMA and DSA

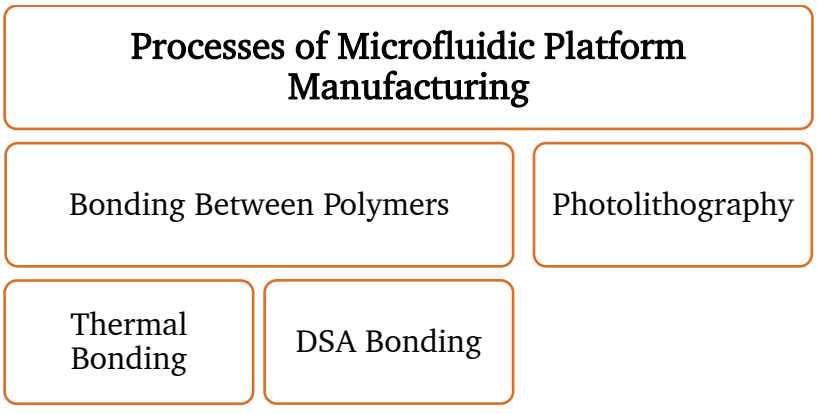


**Figure 2.16** Different kind of processes of microfluidic platform manufacturing

Microfluidic systems can be used in many fields such as health science (miniature liquid analysis), micro laboratory systems, micro mixers, micro coolers, biotechnology (Micro-PCR-Polymerized Chain Reaction), pharmacology. One of the most important components of these systems are micro channels that connect different parts of microfluidic systems. Microchannels act as biological samples or reaction sites, as separators for chromatography or as artificial vessels for microcoolers. There are various technologies for producing micro channels of different geometrical sizes used in microfluidic applications. Among these, it is possible to produce the silicon plate (Si-wafer) used in lithography technique by using large- and large-scale micro channels. These methods should be applied under cleanroom conditions. Within the scope of the project, it was used in the clean room of Gebze Technical University Nanotechnology Institute.

The most widely used lithography method is UV-lithography. Photolithography is the process of shaping the photoresist (photosensitive polymer) coated on a silicon flake (silicon substrate) using a previously prepared mask. The UV light of a given wavelength is transmitted through a mask, the photoresist of this wavelength, which is light-sensitive, laid on a silicon flake. Micro or nano sized shapes on the mask are transferred onto the semiconductor after a series of chemical processes that follow each other. The critical size is directly proportional to the wavelength shaping and the constant 'k', and inversely proportional to the numerical aperture (NA) of the lens. The wave size and number clarity are the values of the technology used as they are the characteristics of the shaping device (stepper) and light source. Therefore, when the value of light (650nm) is taken for standard process conditions of wavelength ‘λ, it is possible to realize smaller shapes than λ⁄2 wavelength.

The environment in which lithography will be performed must be free of particles and sterile. Therefore, lithography is carried out in areas called clean rooms. Clean rooms are classified according to the number of particles larger than one micron in one cubic inch, and most process classes require clean room environments less than 100. The substructures (100mm, 200mm) of the microfluidic based chip are thin circular silicon sheets and are called silicon substone. Since the polymer

(resist) used for coating in the section where the experiments are carried out loses its feature in white light, this section is illuminated using yellow light.

Within the scope of the thesis, different microfluidic chip designs and productions were achieved by lithography.

### 2.2.1 Photolithography for master mold fabrication

Basic lithography techniques were used during microfluidic chip production. Lithography basically consists of masking, coating, curing, exposure, and etching (chemical etching) processes. Nanotechnology Laboratory of Gebze Technical University was used for lithography. UV-lithography procedures were performed with SUUS MicroTec MA6 / BA6 brand device.

Fabrication steps of microfluidic chips:

- Masking Process
- Photoresist Coating with Spin Coater
- Curing Process
- Exposure Process with UV
- Chemical Etching
- Soft (Lithography)

#### 2.2.1.1 Masking Process in Photolithography

Photolithography is based on the coating of a photosensitive chemical material (photoresist) with a desired thickness on a specified surface and then transferring the mask pattern onto the surface by passing ultraviolet light (UV) over a pre-designed photomask. Accordingly, the photomask used for the photolithography process is an important factor in the microfluidic channel fabrication process. In this section, the production process of the chrome photomask used during the photolithography process is explained. The purposes of the use of microstructures on the chromium photomask and the microscope images will be detailed according to the targeted studies in the following sections.

Within the scope of the objectives determined the width of the microfluidic channels produced was designed to be at least 50 $\mu$m and the photomask used in the production phase of these microfluidic channels was determined as “acetate mask”. Despite the restriction of the dimensions of microfluidic channels made with an acetate mask to a minimum of 50 $\mu$m, the microchip was very efficient in the production stage in terms of fabrication quality, economy, and ease of production. However, the new micro fluid channel designs targeted in line with the thesis decrease to 15 $\mu$m. The transfer and design of the design on the chrome-coated glass surface was made with the mask printer device (Heidelberg DWL 66fs) located in Gebze Technical University Micro / Nano Device Production Laboratory.

The first step of production is to create the mask design in a drawing program and transfer it to the mask writing device. It is then transferred to a layer of photoresist coated on the photomask plate. The displayed pattern is developed in the special developer solution of the photoresist to create a template on chrome. Depending on the type of photoresist used, chromium is etched from the areas where UV light is desired to be transferred. After the etching is complete, the remaining photoresist is removed, the plate is cleaned and then stored for use in an optical printer.

In this section, the details of the production stages of the chrome photomask shown in Figure 2.17 are explained.

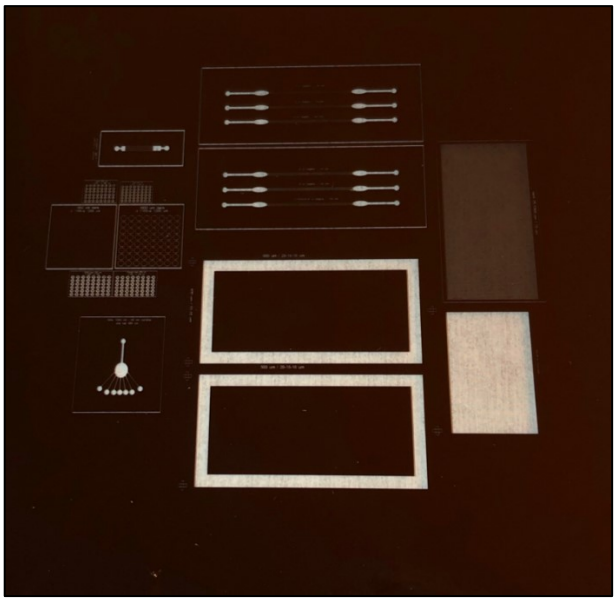

**Figure 2.17** Chrome photomask and microstructures on it are shown.

The 5 x 5 x 0.090-inch plate was cleaned with acetone and isopropyl alcohol for 3 minutes. 110 ° C 20 seconds drying was done on the heater table. AZ 1505 positive photoresist was coated on the plate that was left to be cooled for 10 seconds in line with the parameters of 3000 rpm, 30 sec and 1000 rpm / sec, and then annealing was done on the heating table for 103 minutes. After the cooling process, the plate was placed on the mask printer device (Heidelberg DWL 66fs) and the mask design, previously drawn in the CleWin design program, was transferred to the mask printer program and writing was started. The writing process took approximately 4 hours. After the writing process, the developer chemical was kept in AZ 726 MIF solution for abrasion of the written parts of the AZ 1505 positive photoresist for 55 seconds and at the end of the process the photoresist was transferred to the design. The plate was washed with DI water for 30 seconds. Each microfluid channel design was examined under an optical microscope to check the accuracy of the mask design. The coating of the plate with a positive photoresist ensures the correctness of the writing process after the mask is printed, without protecting the chrome structure yet, and protecting the resist-coated areas during the etching process of the chromium on the mask. Thus, only chromium in places not covered with resist will be worn and transferred to the design mask.

While the abrasion of the chromium material is not recyclable, the return of the photoresist coated on the chromium is abraded with acetone. In case of any misspelling, all photoresist is removed with acetone and all processes are restarted. In order to etch the chrome parts of the plate, which is controlled correctly, it is kept in chrome abrasive chemical for 100 seconds. Thus, in line with the designs of the designed microfluidic channels, the chrome material on the glass was abraded and the glass was made transparent. The plate was cleaned with DI water for 30 seconds and dried with nitrogen gas. Despite the possibility of residual photoresist coating on it, it was kept in AZ 1505 solvent (remover) for 5 minutes at 80 ° C. Chromium cleaned with acetone and isopropyl was dried with photomask nitrogen gas. As a result of all these processes, the chrome photomask special box, which is ready for use, has been kept in a convenient way for continuous use. Chrome photomask production process is shown in Figure 2.18.

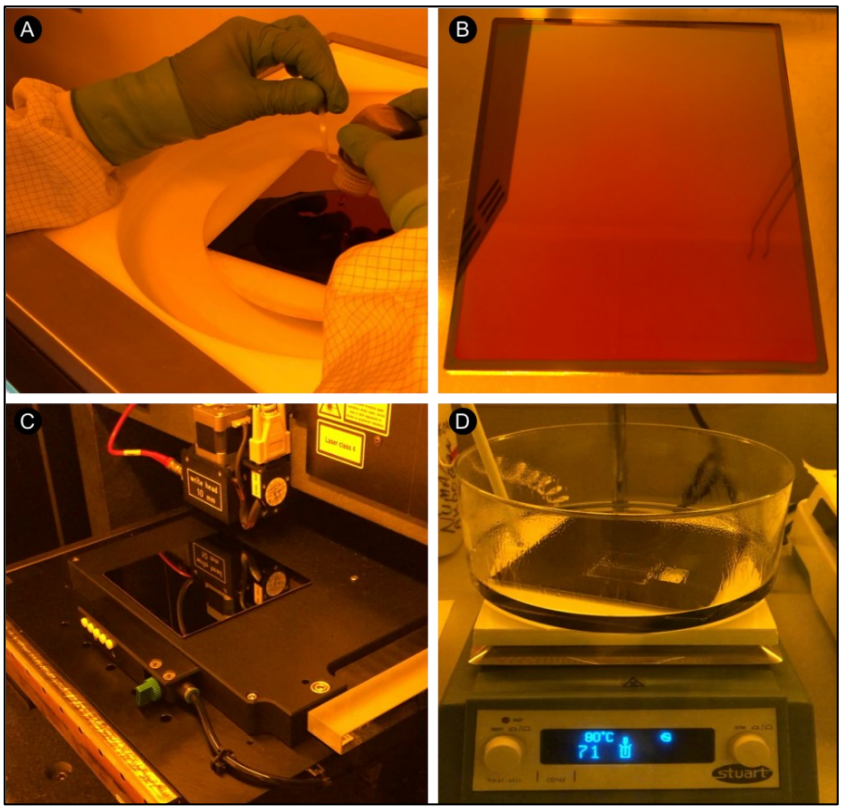


**Figure 2.18** Chrome photomask production steps are shown. A) Placing the cleaned chrome photomask in the rotating coating device and dropping the AZ 1505 positive photoresist B) AZ 1505 photoresist coated chrome photomask

representation C) AZ 1505 photoresist-coated chrome photomask placed in the mask printer device. As a result of all these processes, chrome photomask production has been completed.

#### 2.2.1.2 Photoresist Coating with Spin Coater

Photoresist is a light sensitive polymer coating material. There are two types: positive and negative photoresist. When a positive photoresist is used, the areas of light (UV etc.) of the silicon substrate dissolve during the next chemical etching process and move away from the silicon substrate surface. When the negative photoresist is used, the light-seeing areas harden and do not dissolve during the bathing process, and the photoresist in the non-light area dissolves away from the surface of the silicon substrate. Thus, the negative of the shapes on the mask surface is formed on the silicon substrate surface. Various methods are used to coat the photoresist. These are spin coating, spray coating, coating by dipping method on the vacuum rotary table at a certain speed, and coating by transferring the polymer roller to the surface of the silicon substrate. The method in the thesis is the spin coating method as in Figure 2.19, since it provides a high level of coating homogeneity on the silicon substrate surface.

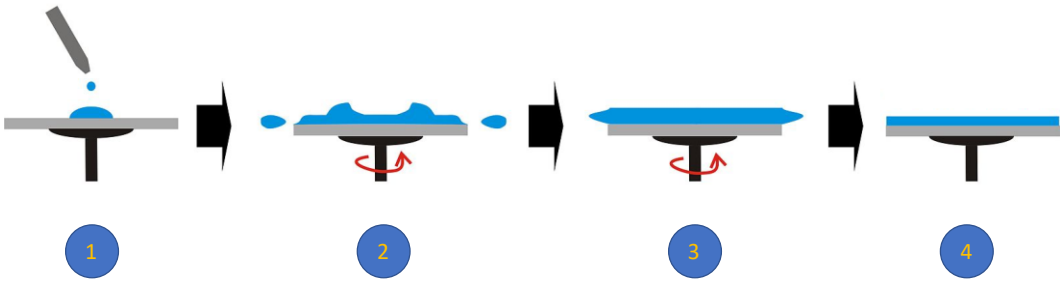


**Figure 2.19** Steps of Photoresist Coating Process

In this method, silicon substrate is placed centered on a vacuum table and the vacuum applied. Silicon substrate is fixed on the table while rotating at high speeds. The photoresist fluid, which is poured into the middle of the silicon substrate with the sprayer, spreads over the entire surface of the silicon substrate with the centrifugal force generated by the rotation of the silicon substrate. spin coating process need to determine the optimum levels of parameters required for

coating. These controlled parameters are; the amount of photoresist, the first rotational speed (rpm), the acceleration to the last rotational speed and how many times it will be repeated. These parameters that we have determined affect the photoresist thickness and the thickness change on the silicon substrate. As caan seen Fig. 2.19, the photoresist coating process is flowed on the silicon substrate in the first step, the second step spreads across the silicon substone with the first rotation speed, and the acceleration determined in the third step is removed from the surface of the photoresist, which is found as an excess on the surface of the silicon substrate.

#### 2.2.1.3 Curing Process

Curing process is carried out by holding the silicon substrate for a certain time in an oven set at a certain temperature or on a vacuum table set at a temperature. After coating, the silicon substrate taken on the vacuum table was exposed to a certain temperature between 45-60 seconds. During this process, the amount of solvent, which is between 80-70% in the structure of the photoresist, drops to around 20-10% and a decrease in the free volume of the resist was observed.

Curing process is carried out in our experiments for the following purposes;

- To improve the adhesion of the photoresist to the surface.
- Avoiding the formation of bubbles caused by $N_2$ gas released during the lithography process by blowing the solvent contained in the photoresist.
- Decreasing the amount of solvent to increase the difference between the dissolution rates of the illuminated and unlit areas during the bathing process.

Curing process also should be done as "post-baking" after exposure. In the final cooking process, the temperature parameters and holding times required for the hot plate vary according to the resistor used. The photoresist used in the thesis is SU-8 2100 (MicroChemical). After the exposure process for the photo resist, it was generally 5 minutes at 65 ° and then 10 minutes at 95 ° hard baking. Duration and temperature values vary according to the thickness of the photoresist used.

Temperature values are determined according to the thickness of the channel to be made and are given in Table 2.4.

#### 2.2.1.4 Exposure Process with UV

In the exposure process, the photoactive substance (diazonaftakinone) in the photoresist structure reacts by exposure to a certain wavelength of light. The parameters that affect the size and profile of the shapes determined on the surface of the silicon substrate determined by the user in the UV device (Figure 2.20) are the lighting dosage and the focal value. The unit of the lighting dosage is Joule/$m^2$, and the device adjusts the amount of energy per unit area by changing the open time of the blades of the curtain that allows the passage of UV light. The duration of the UV-light used in the exposure process is shown in Table-4.

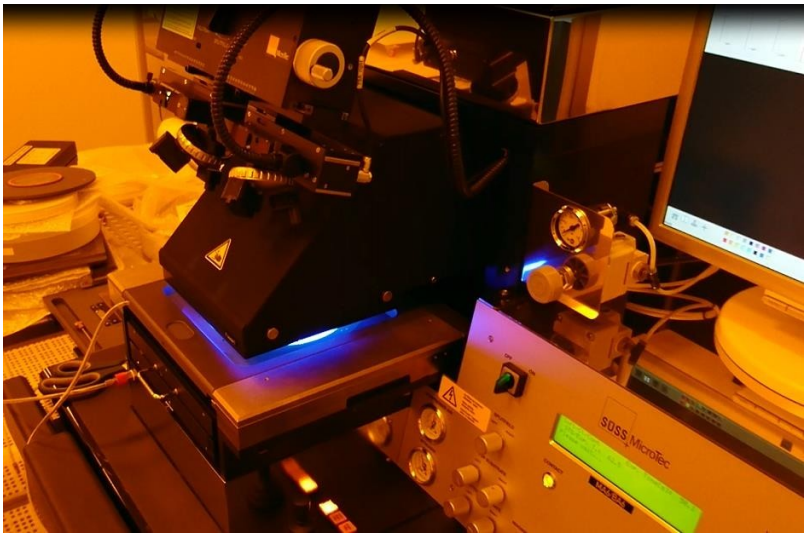


**Figure 2.20** SUSS MicroTec UV Lithography Device

#### 2.2.1.5 Chemical Etching Process

The dissolution of the carboxyl acid formed by the photosensitive photoactive substance (diazo naphthaquinone) UV light exposure in the basic solution in the next step is defined as the chemical etching process. During the chemical etching process, the UV-distorted part passing through the open part of the mask dissolves, while the part corresponding to the closed area of the mask remains on the silicon substrate surface. Thus, the shapes on the mask are transferred to the silicon substrate surface. The final cooking is carried out before chemical etching. One of

the goals of curing process by applying temperature is to reduce the nitrogen produced during shaping and to improve the resist adhesion by reducing the mechanical stress caused by curing before shaping. During the chemical etching process, SU-8 2100 series chemical solvent is used. The product that appears after chemical etching is first bathed with IPA, then Acetone and again with IPA and dried with $N_2$ gas.

### 2.2.1.6 Parameters Used in Photolithography

The fabrication parameters used in the microfluidic chips produced by photolithography are given in Table 2.4. Channel heights vary between 100 $\mu$m and 250 $\mu$m. Parameters based on channel height; The speed and acceleration in spin coating is pre-cooking time, UV-lighting time, final cooking time and chemical etching time.

**Table 2.4** Prescription of photolithography processes made according to channel heights

| Channel Height | Coating speed, acceleration and duration | Pre-Baking Time | UV-Exposure Time | Hard-Baking Time | Chemical Etching Time |
|---|---|---|---|---|---|
| **100 µm** | 1) 500 rpm, 5-10 sec, Acce.:100rpm/sec<br>2) 3000 rpm, 30sec, Acce: 300rpm/sec | 1) 65C 5 min<br>2) 95C 20 min | 9.6 sec | 1) 65C 5 min<br>2) 95C 10 min | 10 dk |
| **200 µm** | 1) 500 rpm, 5-10 sec, Acce.:100rpm/sec<br>2) 1500 rpm, 30 sec, Acce.:300rpm/sec | 1) 65C 6.5min<br>2) 95C 40 min | 12.6 sec | 1) 65C 5 min<br>2) 95C 14 min | 16.5 dk |
| **250 µm** | 1) 500 rpm, 5-10 sec, Acce.:100rpm/sec<br>2) 1100 rpm, 30 sec, Acce.:300rpm/sec | 1) 65C 7 min<br>2) 95C 52.5 min | 14.4 sec | 1) 65C 5 min<br>2) 95C 17.5 min | 18.5 dk |

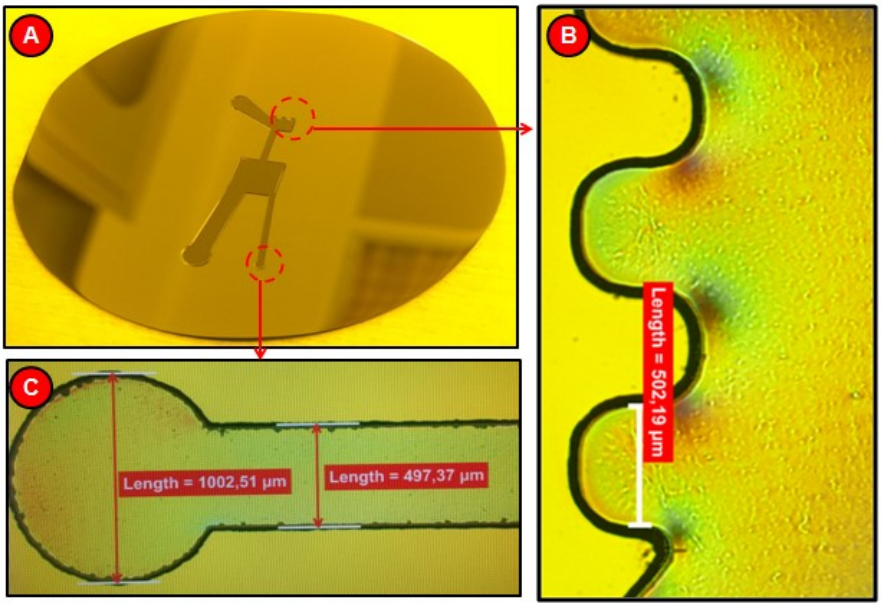


**Figure 2.21** An example of a mold from microfluidic systems produced under the thesis

### 2.2.2 Soft-lithography

After the molding process is completed, microfluidic channels created by photolithography, the next process is to create the channels with soft lithography. Another important step of microfluidic channel fabrication is PDMS mold production. PDMS molds form the basis of the soft lithography technique. Patterns created by the photolithography method on the silicone substrate were transferred to the PDMS structure. The produced PDMS mold is irreversibly connected with glass substrate and the microfluidic channel on which acoustic wave pressures will be created on the cells is completed. PDMS (polydimethylsiloxane) is a silicon-based organic polymer. With its biocompatibility, elastomeric structure, optical visibility, and gas permeability to ensure the viability of the cells, its use in soft lithography technique is very common. PDMS, one of the strongest elastomers in terms of strength, provides reusability and provides multiple experiments on a microfluidic platform [41].

PDMS liquid mixture was prepared in the process. The mixture consists of two materials, the liquid PDMS prepolymer and the curing agent. Air bubbles were formed in the PDMS mixture, which was homogeneously mixed at a ratio of 10: 1

by weight. Since any air bubbles that may occur along the microfluidic channel will hinder the test course, the mixture is kept in the vacuum desiccator for 20 minutes and the air bubbles are removed. Thus, the PDMS polymer mixture is made suitable for pouring onto the silicone substrate. The mold produced by photolithography was treated with isopropyl alcohol, acetone, and again isopropyl alcohol and dried with nitrogen gas, respectively. The cleaned silicone substrate was placed in a petri dish and the PDMS mixture prepared on it was slowly poured. The Petri dish was taken over the heater and the PDMS mixture could solidify at 65 ºC for 3 hours. Solidification takes place based on the reaction between the hydrosilane (SiH) group in the PDMS polymer and the vinyl ($SiCH = CH_2$) group. The PDMS structure, which could cool, was separated from the silicone substrate. The produced PDMS structure has been cut and arranged in accordance with the dimensions to be used. Channel inlet and outlet holes were drilled using a punch. As a result, the PDMS mold of the microfluidic chip design was produced. The construction steps of the PDMS mold are shown in Figure 2.22

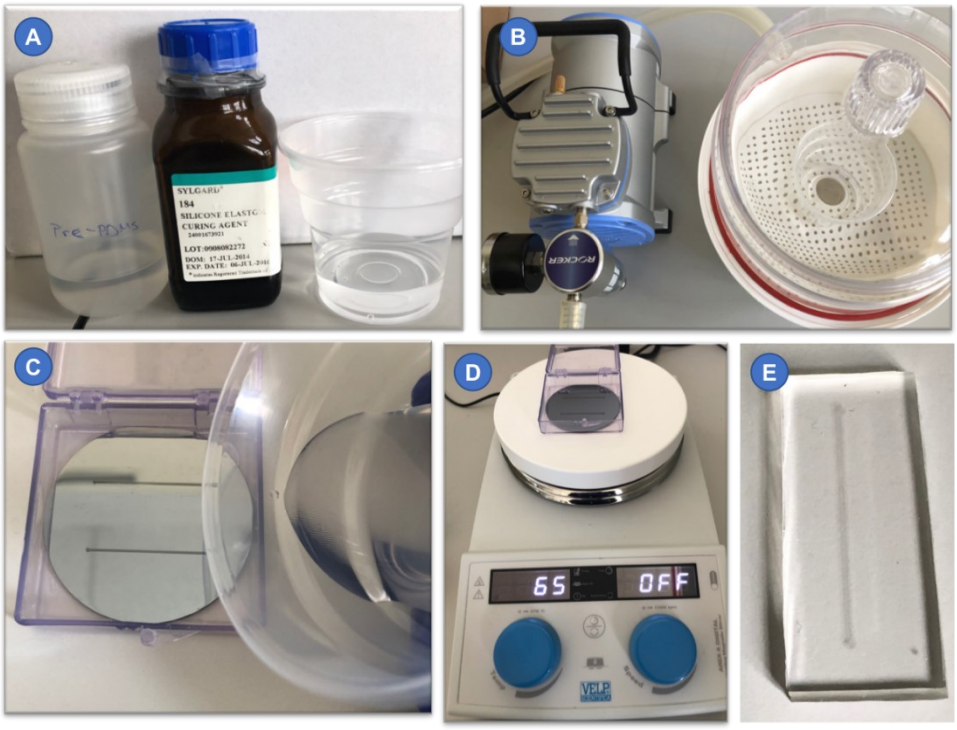


**Figure 2.22** (A) PDMS prepolymer and curing agent were mixed in a 10: 1 ratio. (B) Air bubbles in the mixture were removed by taking a vacuum desiccator. (C)

The mixture was poured on the silicone substrate. (D) It is left to cure for 3 hours at 65 on the heater. (E) PDMS, which is separated from the silicone substrate, has been cut to size to be used, and the channel inlet and outlet holes have been drilled.

For microfluidic channel formation, PDMS mold and glass substrate must be connected irreversibly. The connection of the PDMS mold with the glass surface is provided by creating an oxygen plasma environment in the “Harrick Plasma Cleaner” device shown in Figure 2.23.

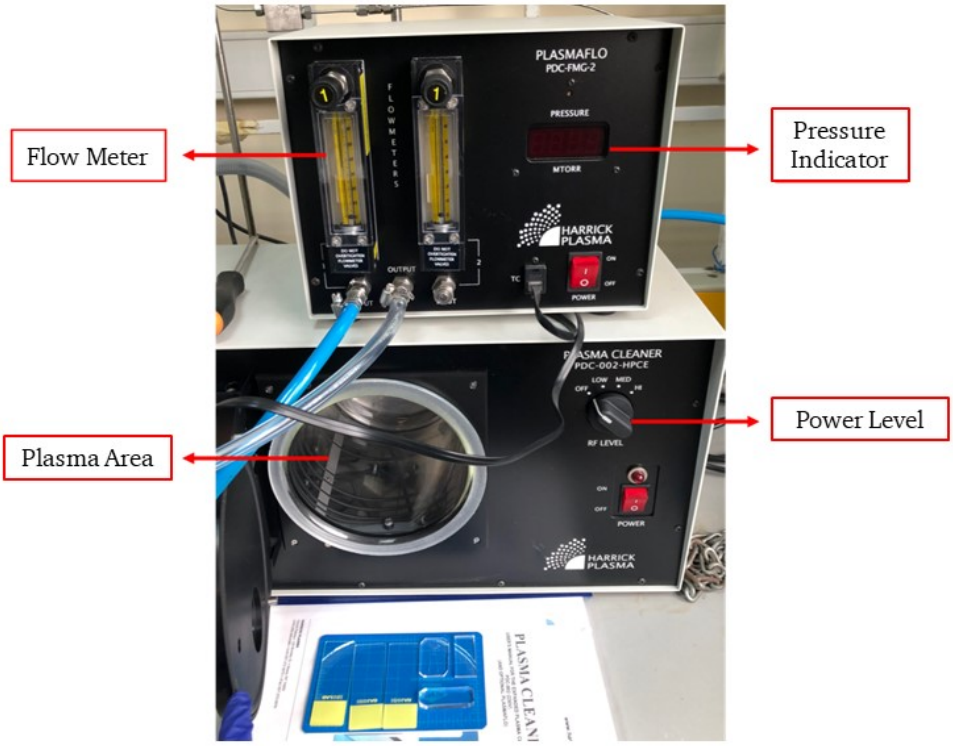


**Figure 2.23** Harrick Plasma Cleaner” device

The PDMS with the hydrophobic surface of the oxygen plasma converges into the Si-OH bonds by combining the Si-CH3 bonds with the oxygen atom on the surface of the mold, thereby making the surface hydrophilic. Since this process is reversible, the surfaces must be contacted with each other within maximum 10 minutes immediately after the oxygen placement, otherwise the surfaces will return to their hydrophobic state. When the glass surface and the PDMS mold are brought into contact with each other, there are Si-O-Si bonds and are irreversibly

connected. Under this foundation, glass substrate and PDMS molded surfaces were placed in the mold device and oxygen plasma was applied at 200 mTorr pressure, 125 sccm flow for 90 seconds. The active surfaces of the parts removed from the plasma medium were brought into contact with each other and a covalent bond was created between the surfaces.

It was left on the heater at 65 ° C for 45 minutes with a weight of over 50 g. Parameters have been determined within the scope of the literature research and if more than the optimum dose is applied, wear is observed on the surfaces. As a result of the process, the PDMS structure was connected irreversibly with the glass surface and the micro fluid channel design was completed. Single channel microfluidic channel is shown in Figure 2.24B.

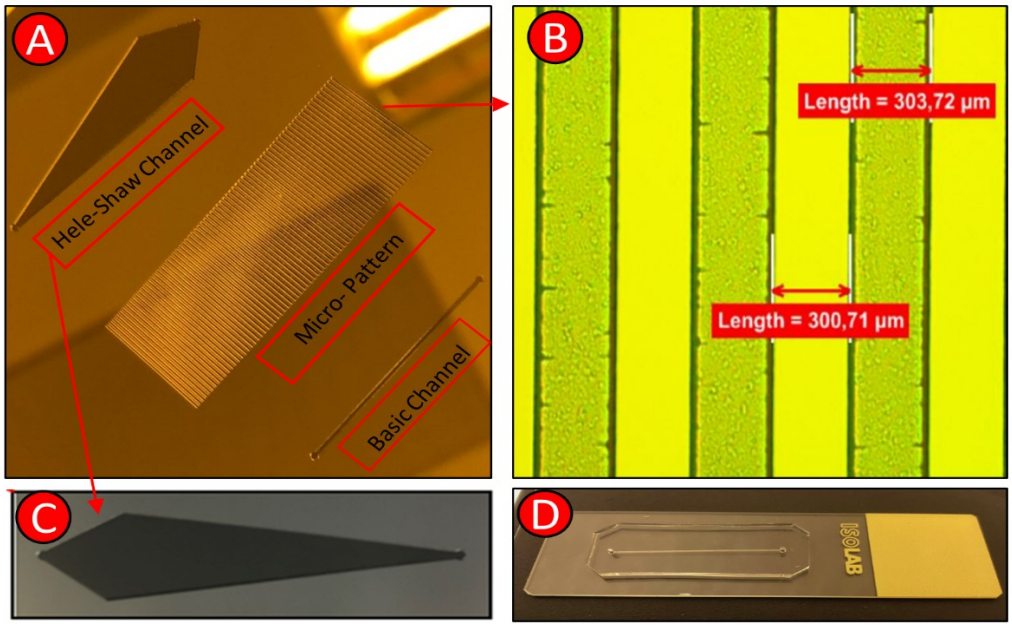


**Figure 2.24** Microstructures and microfluidic chip produced by photolithography within the scope of the thesis

### 2.2.3 Micro-robot Fabrication

A multi-channel microfluidic system has been designed that simulates the activities of cell culture or organ system for their mechanisms and physiological responses. With this system, 2D and 3D cancer tissues were created in the microfluidic channel. Wound models were then created with a micro-robotic

system. Thanks to the wound model created, data on cancer migration, resistance and drug trials were collected. Thus, microfluidic based robotic devices can replace animal models and personalized medicine can be realized.

Our aim in this sub-study is to apply the holographic method in the imaging of cancer cells within the microchip. However, creating a wound model is not a problem that can be solved in today's literature while determining the growth curves of cancerous cells in the microchip. In this way, a very important study is carried out in the visualization of cancer cells integrated with a microfluidic chip, in which acoustic signals will be delivered in accordance with the purpose of our project. In this way, an important lab-on-a chip platform that specialists can use in the diagnosis of cancer in a healthy way without separating from the incubation environment is realized within the scope of this thesis.

Within the scope of the thesis, micro-robots in different designs were produced for the manipulation, detection, and characterization of biological samples in the microfluidic system.

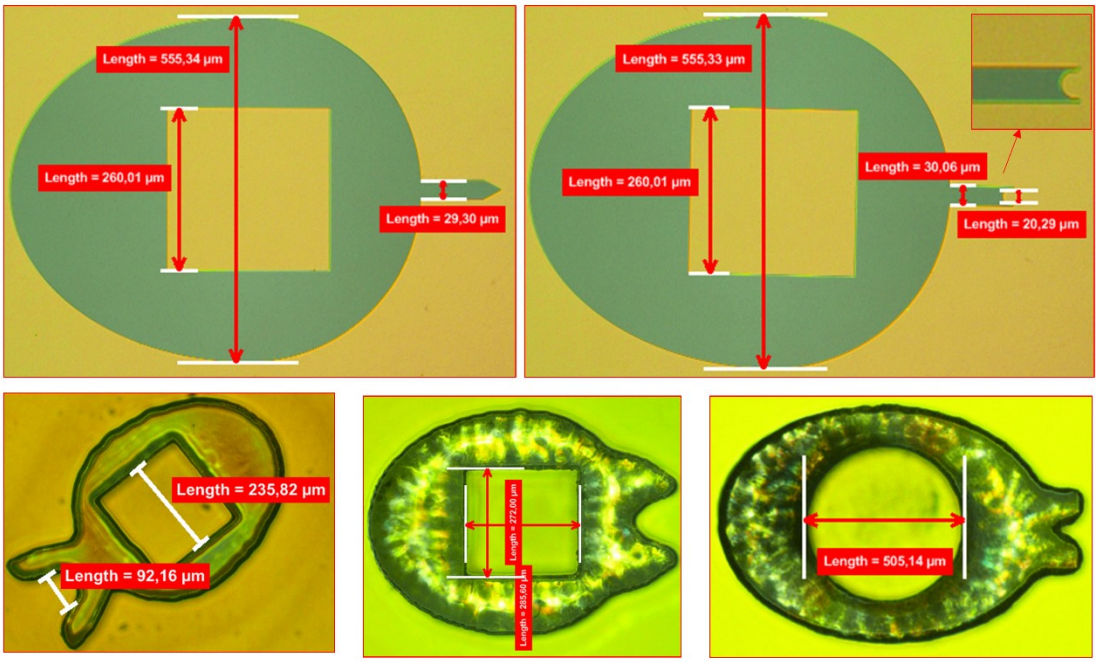


**Figure2.25** Micro-robots produced for different purposes

In this context, a microfluidic channel in which the wound model was created, and an acetate mask were produced for the micro-robot. The width of the

microfluidic channel is 1000 $\mu$m and its height is 500 $\mu$m. The width of the microrobot is 500 $\mu$m and the height is 250 $\mu$m. Entry and exit holes were created for cell culture and micro-robots in the microfluidic channel. The detailed sizing of the microfluidic channel and micro-robot shown in Figure 2.25. Acetate mask and the photoresist mold created by the lithography method. The SU-8 negative photoresist we use is a photoresist that can be used between 100 $\mu$m and 250 $\mu$m heights. However, since the height of the micro-robot used for the wound model is 250 $\mu$m due to the magnet placed, the microfluidic channel must be more than this height. For this reason, the duct height was produced as 500 $\mu$m. In order to use SU-8 negative photoresist at 500 $\mu$m height, the lithography procedure has been changed.

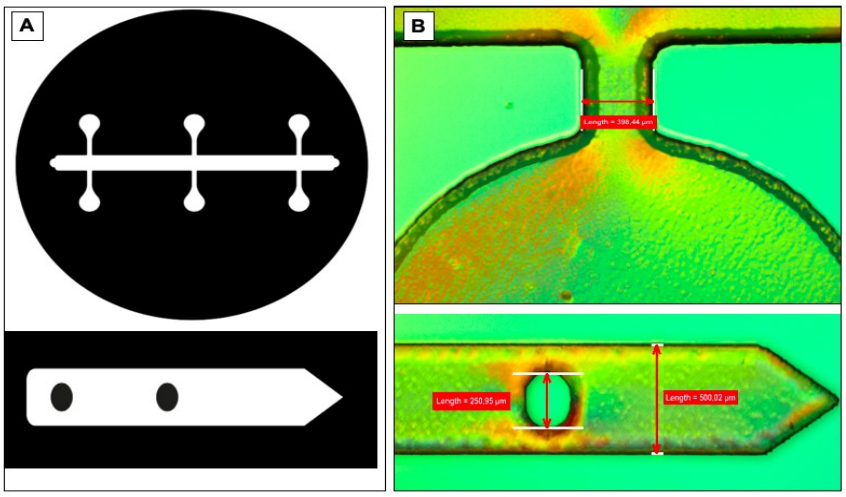


**Şekil 2.26-** A) Microscope image of the microfluidic channel and the transparency mask design of the micro-robot B) The photoresist mold produced by lithography

The parameters applied for a height of 250 $\mu$m were applied twice and pre-baking was carried out between the application. Thus, the first pouring was cured in the pre-baking of 250 $\mu$m and made suitable for the second spin coating process. With this method, the use of the existing photoresist is extended.

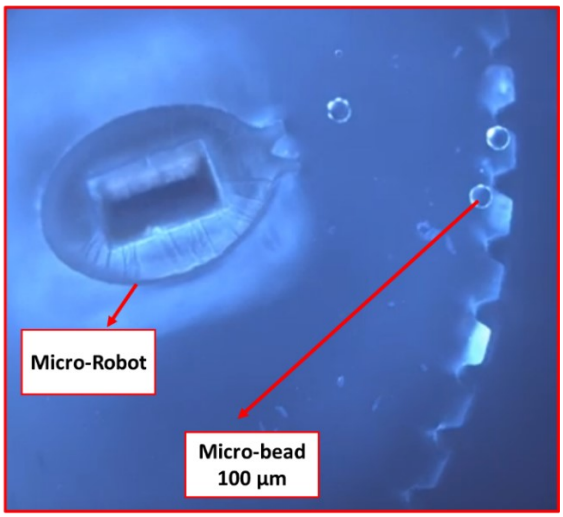


**Figure 2.27** Microscope image of the micro-robot produced by photolithography in the microfluidic channel

## 2.3 Culturing of Different Cancer Cells and Integration into Microfluidic System

Within the scope of the thesis, HCT-116 (Colon Cancer), MDA-MB-231 (Breast Cancer), ONCO-DG-1 (Ovarian Cancer), and HUVEC (Human Umbilical Vein Endothelial Cells) from ATCC (Manassas, VA, USA) were used in the experiments. HCT-116 cell line, MDA-MB-231 116 cell line and ONCO-DG-1 cell line were cultured in McCoy's 5 A, Leibovitz's L-15 Medium, and RPMI 1640 modified liquid medium from Merck with 4.5 mg/mL glucose, 10% fetal bovine serum, and 5% penicillin/streptomycin, respectively. Cells were maintained in an incubator at 37°C and 5% $CO_2$. The medium was changed every three days, and the cells were passed to new flasks upon reaching confluency.

# 3
# APPLICATIONS OF THE DEVELOPED MICROFLUIDIC SYSTEM TO DETERMINE THE MECHANICAL PROPERTIES OF CANCER CELLS

## 3.1 Creating a Wound Model with Micro-Robot in Microfluidic System

Microfluidic systems have been heavily used in micro/nano robotics and biomedical applications. Micro-robots, which are actuated via magnetic forces, are useful for many tasks such as cell manipulation [42-43], drug delivery [44-45], biopsy [46-47], and marking [48-49] within lab-on-a-chip platforms and in vivo applications. In a microfluidic environment, flow characteristics and environmental effects, related to acting forces on a microrobot change with decreasing dimensions. A variety of approaches have been devised to overcome such challenges and provide an optimal method of propulsion for the micro-robots to move inside microfluidic environments, but all have different kinds of limitations. Previous studies have suggested the use of electrostatically powered scratch drive actuators [50] which needs a patterned surface that consists of an array of insulated electrodes. Other studies make use of the stick-slip motion, that is caused by a rocking movement of the micro-robot, in order to move the robot forward in both fluidic and dry environments [51], [52]. Although high speeds and power output is achieved via this approach, it is only feasible for 2D movement on a smooth surface. Use of stationary electromagnets for 5 DOF movement of the micro-robot by manipulating the gradient of the magnetic field generated by the electromagnets situated around the platform is also studied [53]. This system requires eight bulky electromagnets integrated with a cooling system and provides a limited working area. Other studies have investigated the use of Helmholtz and Maxwell coil pairs for both the propulsion and rotation of the

micro-robots [54], [55]. However, these systems require rather sizable electromagnet pairs and thus are restrained in their configurations and limitations. Sitti et al. have describe a method to code complex materials in three dimensions with tunable structural, morphological, and chemical features using an untethered magnetic micro-robot to be introduced to arbitrary microfluidic environments for remote two-three-dimensional manipulation [55]. Kim S. et all. have demonstrated multifunctional microrobots for targeted cell delivery using 3D laser lithography. The microrobots were coated with Nickel and Titanium layers as magnetic and biocompatible materials, respectively. The fabricated porous 3D structures were used for 3D cell cultures of HEK 293 cells. In addition, dynamic cell culture, drug trials, wound models, etc. created in microfluidic systems have become increasingly important. Examining wound healing is a vital process in terms of developing treatments. Wound healing dynamics depend on physical and chemical properties of the tissue; therefore, these examinations should be performed for each and every type of tissue. Wound healing abides four stages which are listed as follows: hemostasis and inflammation, chemotaxis and activation, proliferative phase (epithelization, angiogenesis, and provisional matrix formation), maturation and remodeling [56]. If these phases aren't executed properly, wounds may lead to serious diseases. Underappreciation of the inherent complexity of the healing wound has led to the failure of monotherapies, with no significant reduction in wound healing times [57]. Thus, it is crucial to examine wound healing process in detail. In order for that, several methods for wound healing assay were introduced such as comparison of wound healing processes in a petri dish and a microfluidic environment [58-59] which concludes to the claim that microfluidic environment has closer conditions to in vivo than any other method, using PDMS (polydimethylsiloxane)-based microfluidic devices [59], and advantages and disadvantages of using microrobots in cell culture [60]. While most of these studies executes experiments in 2-dimesional (2D) cell culture, it is strongly implied in several more studies [61-62] that 3D cell culture offers way more realistic characteristics in terms of simulating a real animal tissue. Cells cultured as 3D models exhibit features that are closer to the complex in vivo

conditions [63]. The 3D culture models have proven to be more realistic for translating the study findings for in vivo applications. While cell lines provide us with excellent homogenous study material, culturing them as 3D models induces them to behave in a manner that is a step closer to the natural conditions [64].

In this study, we describe a 2D and 3D wound healing assay with wound generated via specially designed and magnetically manipulated micro-robot and observed with a holographic imaging setup. Dynamic three-dimensional cell culture was created in the microfluidic channel which is produced by soft lithography. In this 3D tissue model, a wound was created with a magnetically manipulated micro-robot. Our proposed system offers a 3D wound healing assay created with a microrobot especially designed to ensure uniformity. A uniform wound assay is necessary in terms of accurate results in the healing factors. Using a magnetically manipulated microrobot instead of a pipette tip etc. as opposed to counterpart systems mentioned earlier in the introduction establishes an advanced level of control over the geometry of the wound. The wound model was monitored by holographic image tracking system for 3D healing and cell migration every 12 hours. Particularly, the 3D cell culture created in the microchannel using microgel. After the microchannel is entirely coated with cells, the biocompatible microrobot was placed inside the channel, moving towards the center of the channel, and creating a uniform hollow wound by layering cells from the center to outlet. For the monitoring system, we use the phase-changing incline Mach-Zehnder interferometer technique. With this holographic system, the migration and healing of the cells were monitored in real time and in 3-dimensions. HUVECs (Human Umbilical Vein Endothelial Cells) and HCT-116 (Colon Cancer) were chosen as the appropriate cancer cell line for the experiments to cross-check the results. Upon the experiments conducted on the monitoring system and the different abilities of the microrobot, it has compared sufficient in terms of success metrics. Finally, we have determined that our novel 3D monitoring system could provide new horizons for the study of wound healing and likewise cell processes.

### 3.1.1 Experimental Setup

There are two main setups regarding to wounding. First one is the micro-robotic setup where wounding happens within 2D and 3D cell cultures inside microfluidic channels. For this setup, first thing we did was to culture 2D and 3D cells in microfluidic channels. Secondly, magnetically manipulated microrobot is released from the inlet and we generated a wound across the channel. The robot is controlled via NdFeB (neodymium) integrated onto a 6-axis Hexapod. The NdFeB magnet functions as a control magnet in the system connected to the 6-axis. Lastly, microrobot is removed from the outlet. Second setup consists of holographic imaging system. After the wounding, we observed the healing in an interferometer in 3D.

#### 3.1.1.1 Microfluidic platform design and fabrication

We have designed a microfluidic platform that accommodates cancer cells and optimize their sustained viability and growth. To accomplish this, we first theoretically evaluated and characterized the physical environmental parameters such as channel designs, flow rate and patterns in order to assess and predict their influences on the cells. The proposed chip was fabricated through standard soft-lithography techniques shown in Fig.3.1, which included the following a series of steps: silicon wafer cleaning, SU-8 spin coating, UV exposure, developing in PGMEA. Then, the formed mold is passed to the soft-lithography step and 10: 1 PDMS are poured and baked. Oxygen is exposed to plasma and bonded. The microfluidic device in PDMS (Dow Corning) elastomer was fabricated by replica molding from an SU-8 (Micro Chem)/silicon master based on a ratio of 10:1 to curing agent. The master mold was produced by ultraviolet (UV) lithography. After pouring PDMS on a mold, the mixture was degassed in a vacuum chamber for air bubble removal and cured at 80°C for 1 hour in the oven. The devices were then cut out by a razor blade; the fluidic connection ports were punched, and bonding to a glass slide was done after oxygen plasma of both surfaces and conformal contact (Harrick Plasma cleaner/sterilizer, 4 mbar, 120 s). Assembly

quality control and characterization were done by optical 3D profilometry (VK-X250, KEYENCE, Germany).

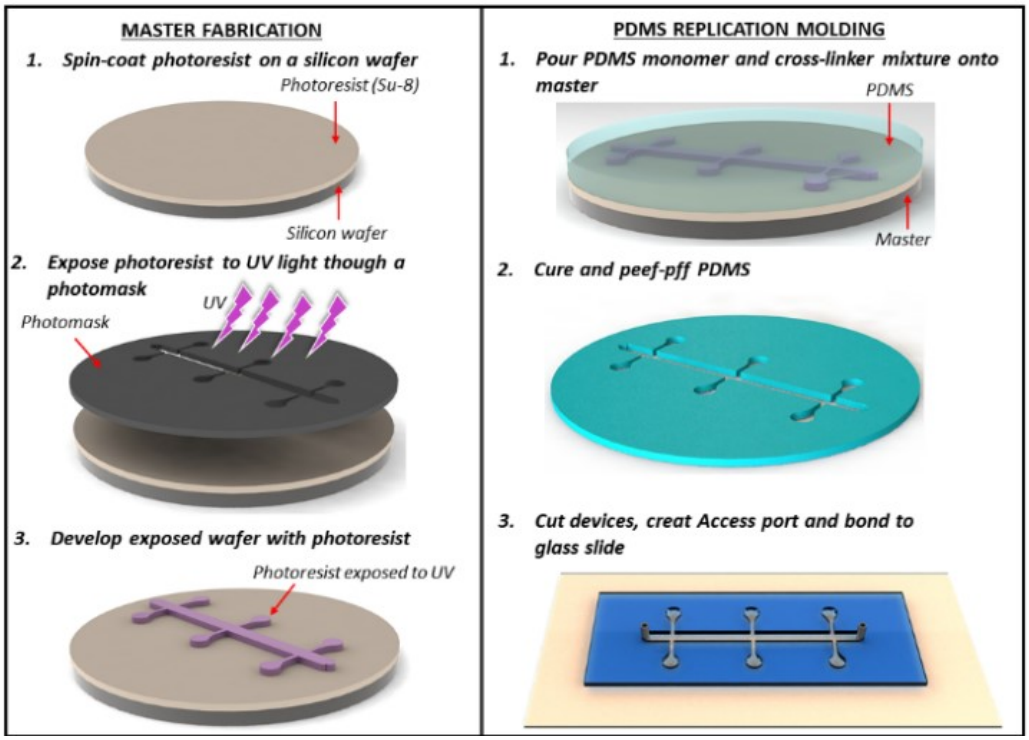


**Figure 3.1** Microfluidic platform design and fabrication

### 3.1.1.2 Micro-robot Fabrication

Micro-robot fabrication steps are start with AZ 1505, a positive photoresist is firstly coated onto a substrate surface as a sacrificial layer (Micro Chemicals GmbH, Ulm, Germany). After that, a negative adhesive film with a thickness of 250 micron was coated on sacrificial layer by spin coater at 1100 rpm. The exposure process on film is applied and then final polymer micro-robot body was obtained by the pattern development process. As the last step, neodymium (NdFeB) circular permanent magnet (N52 grade) with the dimensions of 0.25 mm x 0.25 mm (diameter-thickness) is coated with PDA (Polydopamine). Then PDA-coated biocompatible permanent magnet was assembled in micro-robot body 2D and 3D cell culture process.

### 3.1.1.3 Cell Culture

HCT-116 (Colon Cancer) cell lines from ATCC (Manassas, VA, USA) were used for experiments. Cells were cultured in McCoy's 5 A modified liquid medium from Merck with 4.5 mg/mL glucose, 10% fetal bovine serum, and 5% penicillin/streptomycin. Cells were maintained in an incubator at 37°C and 5% CO2. The medium was changed every three days, and the cells were passaged to new flasks upon reaching confluence. Cells suspended with Corning Matrigel were transferred to microfluidic channels after trypsinization Corning® Matrigel® matrix is an ECM (Extracellular Matrix)-based natural hydrogel that has been extensively used for 3D cell cultures in vitro and in vivo. It allows the cells to grow in three dimensions. Matrigel matrix, or an equivalent, which demonstrated the enabling power of 3D cell culture for creating in vivo-like model systems and the importance of integrin signaling in cancer. After 3 hours of incubation, the microfluidic system is incubated at 37°C and 5% $CO_2$ atmosphere. Cells were exposed to 5 µm/s continuous laminar fluid flow for up to 7 days.

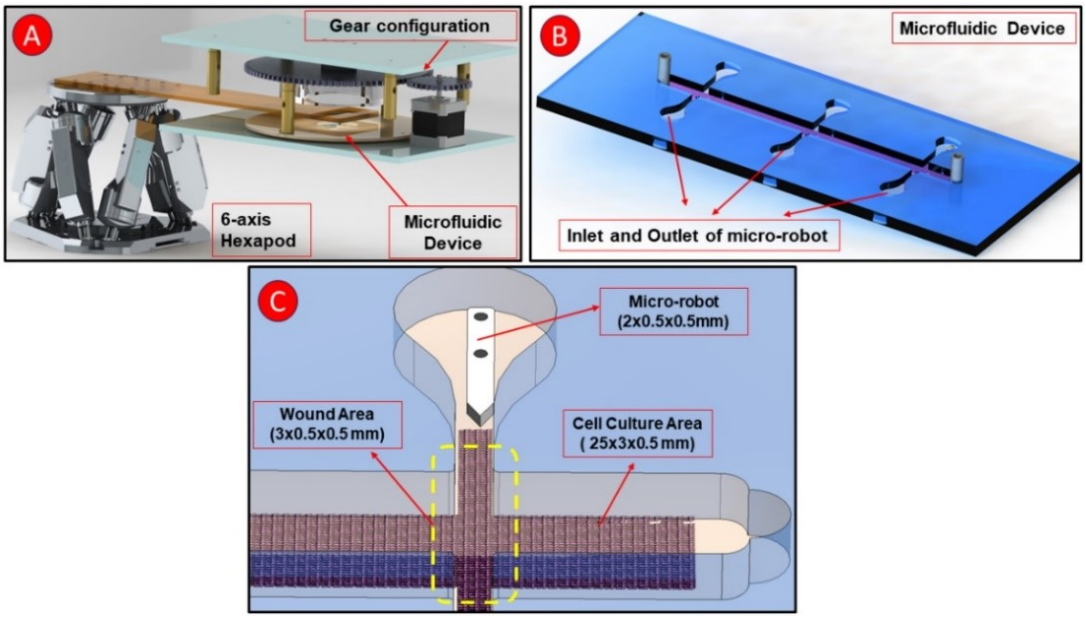


**Figure 3.2** Wound Model Experimental setup. Fig. A: Mechanical system for the wound model. Precise control of the robot in the microfluidic channel integrated into 6- axis Hexapod. By means of gear configuration, micro-robot can also yaw axis. Fig. B: Microfluidic channel designed for the wound model. This

microfluidic device is examined through three wound models created at the same time. Micro-robot is removed after the wounding process. Fig. C: Micro-robot that generated the wound model in cell culture medium.

#### 3.1.1.4 Mathematical Model

The manipulation technique proposed in this study is based on a ferromagnetic micro-robot inside a microfluidic chip. For the control of the micro-robot inside the channel, we used a driving magnet attached to the 6-axis Hexapod and a micro magnet integrated into the micro-robot. The magnets are made of NdFeB with remanence magnetic field strength of 1.37 T for a volume of $1cm^3$. The basis of the proposed mathematical system was concentration of the magnetic field force lines on the micro-robot and the formation of a force vector on the horizontal axis of the micro-robot. A detailed view of the magnetic mechanism is shown in Figure 3.3.

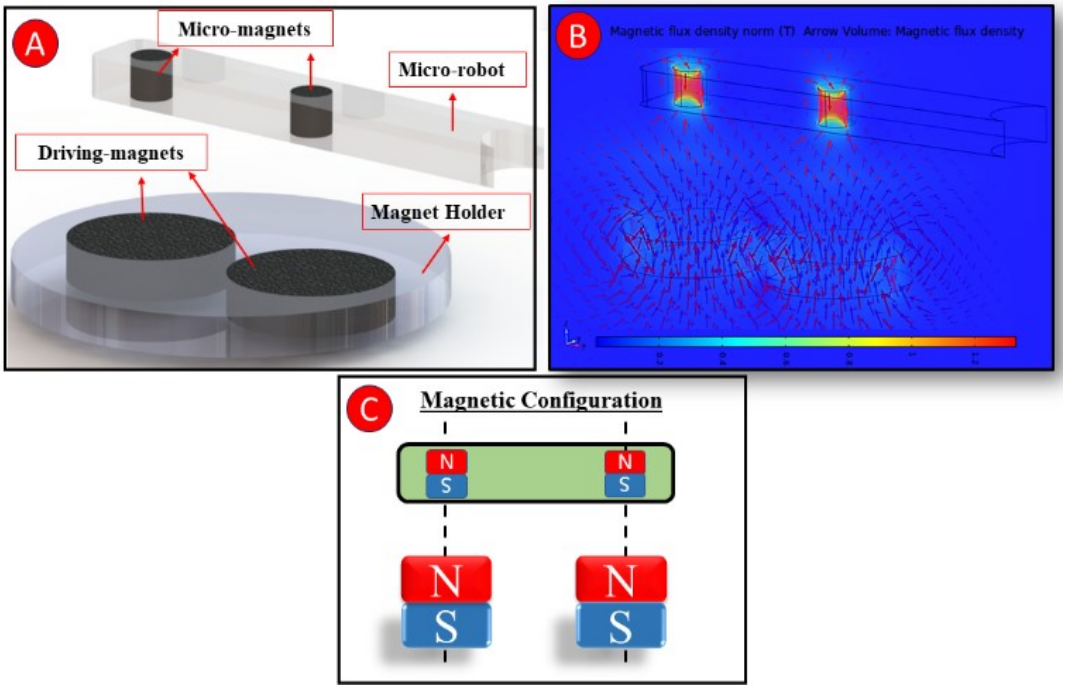


**Figure 3.3** Concept of the micro-robot manipulation. Fig.3.3 B Magnetic flux density between the driver-magnets and micro-magnets in the micro-robot. Fig3C Magnetization of the magnets is in the Z axis.

The magnetic force on the robot originates from the attractive force between the driving magnets and the ferromagnets inside the micro-robot. As a result of the magnetic analysis performed in Fig.3.3 B, the magnetic force acting on the robot on the x-axis was calculated as 106.5 $\mu$N. A gear system is designed to magnetically manipulate the micro-robot. Driving magnets is integrated onto the Hexapod and microfluidic channel is placed onto the gear system. The robot can move along x-axis while yawing through the gear system. While the robot is generating the wound, adhesive forces cause deviation in robot's direction. Because of that, control of the yaw axis is crucial in terms of angle stabilization.

#### 3.1.1.5 Monitor Cell Growth Process Using Holographic System

For almost all cell manipulation tasks, the morphological structure of the manipulated cells is a critical parameter. Cell morphology is an important determinant of the cell genotype and determines many of its characteristics including its surface adhesion behavior its intra cellular signaling pathway regulation and its membrane permeability. It is also a stronger indicator of the class a cell belongs to, compared to classical light microscopy techniques [65]. We investigate the use of morphological information in cell healing operations. Assessment of the cell shape and cell-surface adhesion helps better understand how to direct the actions of the migration. Holographic system is an emerging high-resolution imaging technique that offers real-time imaging and quantitative measurements of physiological parameters without any staining or labeling of cells. A key feature of holographic system is the ability to study cell morphological changes associated with differentiation. Phase shifting inline Mach-Zehnder interferometry technique was used for healing and migration imaging. Mach-Zehnder interferometer is a 3D reconstruction method based on the interference of a signal wave which contains the wavefield transmitted from the observed sample and a reference wave which contains the wavefield of the original coherent light source. A laser beam is divided into two beams by use of a beam splitter. One beam is the reference beam which travels through a compensating chamber which is a microchip filled with an empty medium and the other beam is the object beam

which travels through a microfluidic device filled with a medium which contains the cancer cell culture to be observed. These two beams are then combined into a single laser beam which contains the fringe patterns due to the interferometry of the reference and the object beam. The intensity distribution of a given interferogram is,

$$Lj(x,y) = A^2{}_0(x,y) + A^2{}_r + 2A_0(x,y)A_r cos[\theta o(x,y) - \delta j]$$

The phase information of the sample can be reconstructed by translating the reference wave and solving the set of linear equations that form taking the Fresnel transformation of the complex wavefield that is recorded via an image sensor [66]. To decrease the computational burden of the Fresnel transform, [67] proposed a Fresnel approximation method based on stepwise shifting of the reference wave. In this study we follow this approach using a PZT actuator for shifting the phase of the reference wave.

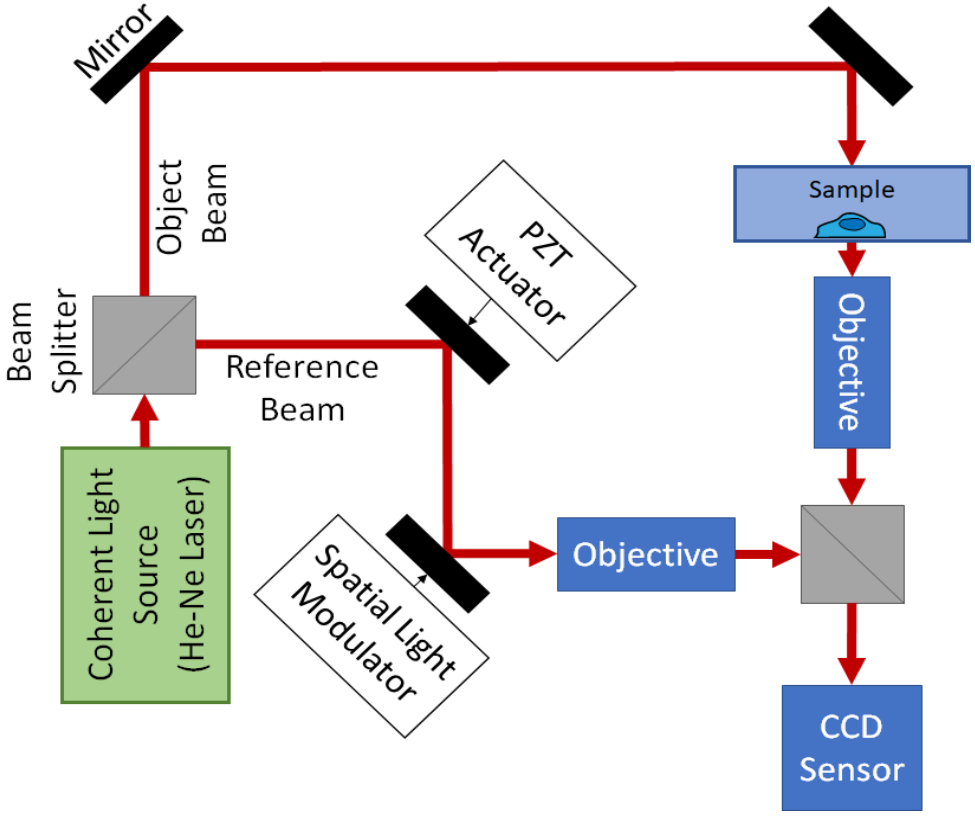


**Figure 3.4** Inline phase shifting Mach-Zehnder interferometer used for acquiring the depth map of the operation environment.

### 3.1.2 Experiments

HCT-116 colon cancer cell line was used during the experiments. HUVECs and HCT-116 cell line is used during the experiments while HCT-116 assay is narrated since the process is highly similar. For the wound model, the micro-robot was magnetically manipulated to form the wound model. This wound model was then followed by holographic system. The experimental setup of the holographic system is shown in Fig.3.5.

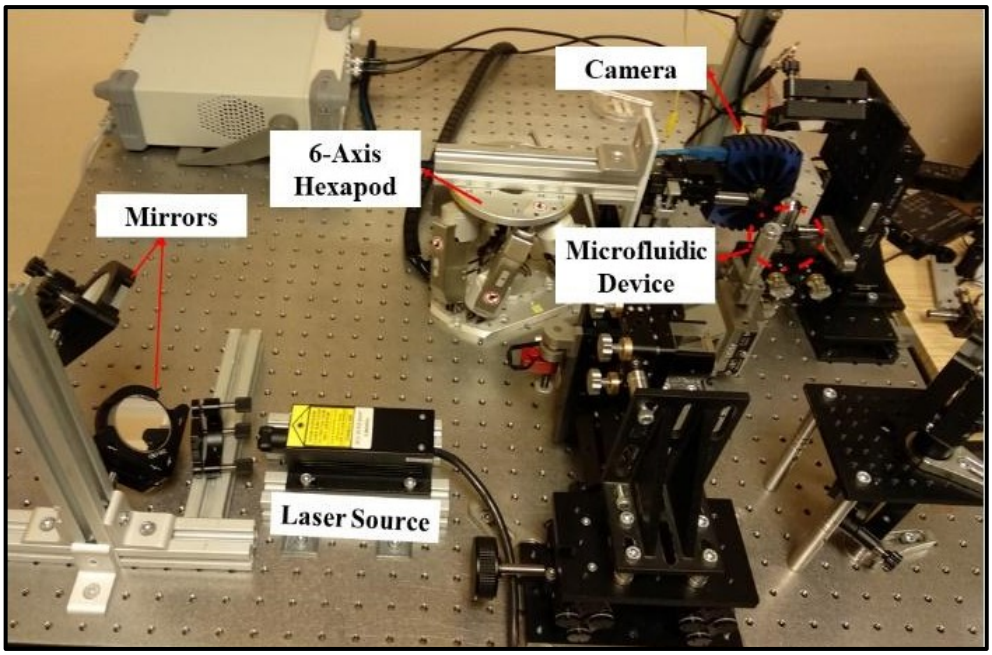


**Figure 3.5** Inline phase shifting Mach-Zehnder interferometer used for acquiring the depth map of the operation environment.

Firstly, cells were cultured in the microfluidic channel. Cells were cultured in microfluidic channels by three-dimensional and two-dimensional cell culture methods. Fig.3.6 shows examples of two-dimensional and three-dimensional cell culture in a microfluidic device.

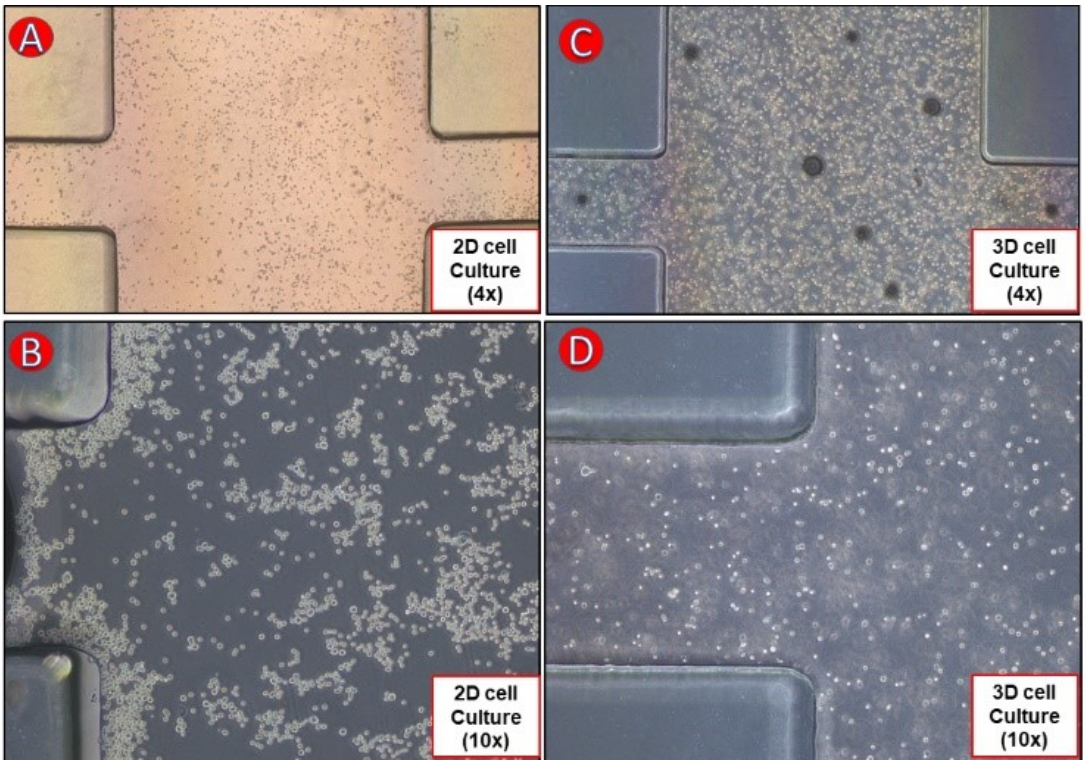


**Figure 3.6** For the 2D and 3D wound model, the microfluidic channel image was imaged 4X magnification (A and C) and 10X magnification (B and D). Figure A and C shows HCT-116 cell line while Figure B and D shows HUVEC cell line. As can be seen from Figure A and B, cells can be observed in single layer in 2D cell culture in microfluidic channel, whereas in Figure C and D cell culture cells have grown in multiple layers.

After the cells were fully adhered to the surface and grown, the wound model was created by the micro-robot. Fig.3.7 shows the micro-robotic wound model. The HCT-116 colon cancer cell line and HUVEC (Human umbilical vein endothelial cell) was used to construct the wound model. Cells completely covering the surface were scraped with micro-robot. Thus, a wound model was created. After the wound model was created with micro-robot, wound healing was monitored by holographic system.

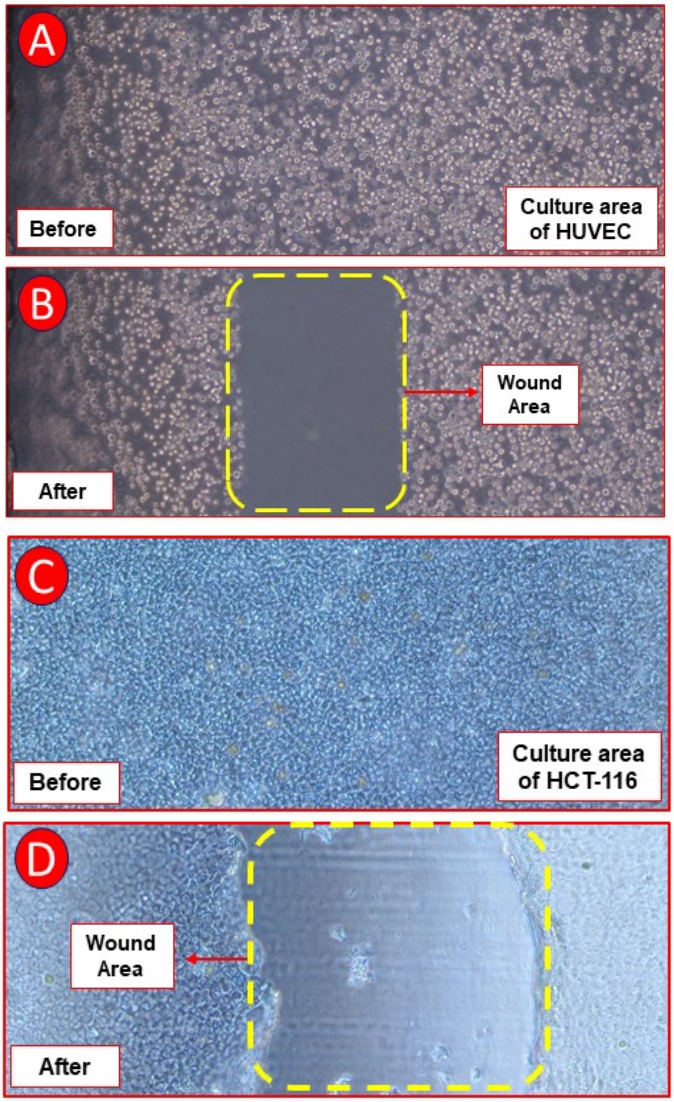


**Figure 3.7** 2D and 3D wound model created with a magnetically manipulated micro-robot.

Thanks to the holographic system, cell growth, migration and drug interactions can be monitored in the incubator environment in real time.

### 3.1.3 Results and Discussion

In this sub-study, the results obtained from each of our experiments. Fig. 3.8 shows the holographic images of the wound model which is generated with micro-robot. The positioning accuracy of the micro manipulator is approximately 0.5 $\mu$m which provides us enough accuracy for creating a wound in the microfluidic device. Through these experiments we see that the deformation rate remains below 8%. We also observed that while the more adhesive cells have higher

deformation rates, less adhesive cells have negligible deformation. In the systems created for the two- dimensional and three-dimensional wound model, the micro-robot was difficult to move the gel out of the microfluidic system. For this purpose, a system design which increases the lateral forces of the micro-robot will be made.

Finally, we describe a 2D and 3D wound healing assay with wound generated via specially designed and magnetically manipulated micro-robot and observed with a holographic imaging setup. Dynamic three-dimensional and two-dimensional cell culture was created in the microfluidic channel which is produced by soft lithography. In this 3D tissue model, a wound was created with a magnetically manipulated micro-robot. The wound model was monitored by holographic image tracking system for 3D healing and cell migration every 12 hours. Particularly, the 3D cell culture created in the microchannel using microgel. After the microchannel is entirely coated with cells, the biocompatible microrobot was placed inside the channel, moving towards the center of the channel, and creating a uniform hollow wound by layering cells from the center to outlet. For the monitoring system, we use the phase-changing incline Mach-Zehnder interferometer technique. With this holographic system, the migration and healing of the cells were monitored in real time and in 3-dimensions. Finally, we have determined that our novel 3D-monitoring system could provide new horizons for the study of wound healing and likewise cell processes.

This method, which is a new method for cancer research and best mimics the in vivo environment, will make a great contribution to the literature. Thanks to the wound model, data about cancer migration, resistance and drug trials were collected. Thus, the substitution of animal models of microfluidic-based robotic devices and personalized medicine can be realized.

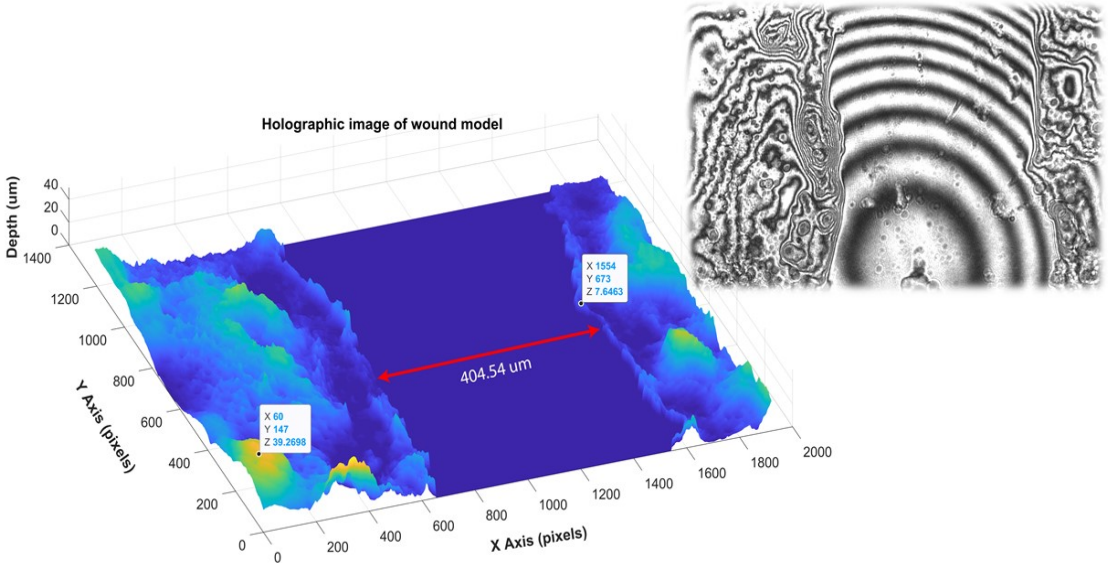


**Figure 3.8** Holographic images of the wound model which is generated with micro-robot. In the hologram image, the depth information is displayed on the z-axis. The size of the wound model is the same as the length of the arm of the micro-robot. The size of the wound pattern formed at 400 $\mu$m is also shown.

## 3.2 Mechanical Characterization of Cancer Cells on-Chip Using Surface Acoustic Wave

Recently, studies have intensified on the removal of the characteristic of cells with the developing technology. Various detection methods have been developed using the characteristic of cells. Examples are flow cytometry, imaging cytometry, and photoacoustic. Classification of cells using these methods becomes an important tool used in biological and biomedical research and clinical treatment. This frequency corresponds to the natural frequency of the surface to which the cells are attached, since the acoustic waves can propagate most effectively in the environment. Since the compressibility, mass, size and density of different cells will be different, they are also affected by acoustic surface waves. In addition, the size of the adhesion force, which is one of the most important forces affecting the cell and its speed, depends on the characteristic parameters of the cells. Due to

these effects, the mechanical stiffness of the cells can be detected using this method.

The aim of this study is to develop a new detection technique in a microfluidic device that will be used to measure the change in cancerous cells in the structure of cell stiffness at a single-cell level. The ability of cancer cells to occupy, starting from the basement membrane, is defined as a critical step during metastasis. The increase in protease secretion that triggers basal membrane disruption causes changes in cancer cells' cytoskeleton architecture. This can increase the mechanical flexibility structure of cancerous cells by up to 70% [68]. The hardness of the cancerous cell is a mechanical change and can be determined by examining the mechanical changes in the cell exoskeleton. Most of the methods used in the literature are performed by external mechanical simulation (AFM probe, micro-pipette aspiration) [69].

Within the scope of the thesis, the mechanical deformation occurring on the cell using acoustic pressure waves in the developed microfluidic system was measured with the "Quantitative Phase Imaging" technique. With the images obtained, the cell stiffness can be measured and the mechanical properties of cancerous cells are characterized. With this method, in which direct mechanical interaction is not used, it is aimed to display the characteristic vibration patterns created by the acoustic effect on the cancerous cell. Thus, a great contribution to the literature has been made in studies on the structure and formation of cancerous cells. A new method has been proposed to monitor cancer patients individually and to monitor the disease in a real-time, non-invasive method. It has been a useful method for Liquid Biopsies and an approach to increase patient treatment success. [70].

The developed microfluidic system is a "non-destructive analysis method" that can measure ultrasonic waves at certain frequencies by sending them over the cell [71]. It is a label-free technique that can measure using the phase and amplitude shifts in the light that the pressure waves will generate on the cell. The system developed within the scope of the thesis has been tried on three different cancer

cells selected due to its clinical importance to be placed in microfluidic chips in-vitro conditions.

### 3.2.1 Theory and Mathematical Model of Acoustic System

In the thesis, it is based on deforming the mechanical properties of the cells using acoustic waves in microfluidic channels and holographically displaying and detecting their movements under acoustic forces. Thanks to constituted acoustic experimental setup, modeling the acoustic wave propagation and the forces that these waves created on the cancer cells is investigated.

A sine acoustic wave moving in the X-axis can be expressed as a wave function equation (3.1) that provides the wave equation (3.2) [72]. This equation indicates that the acoustic wave can be modeled as a decay that travels along an axis at a certain wave velocity [73]. In fluid environments, these distortions can only be observed longitudinally, while in solid environments they can be observed longitudinally or laterally. This is because the resistance of fluid media to shear stress is very low.

$$y(x,t) = A \cdot \sin(\omega t - kx) \tag{3.1}$$

$$\frac{\partial^2 y(x,t)}{\partial x^2} = \frac{1}{c^2} \cdot \frac{\partial^2 y(x,t)}{\partial t^2} \tag{3.2}$$

Here, $y$ displacement, $x$ position, $t$ time, $A$ wave amplitude, $\omega$ angular frequency, $k$ wave number ($\lambda$ dalga boyu ise $2\pi/\lambda$), $c$ wave velocity.

As a result of the overlap of two acoustic waves with equal amplitude and frequency, a wave form called standing wave occurs. Stationary waves do not transfer energy unlike moving waves. In other words, net energy transport in all axes is equal to zero. These waves have node points without particle motion and anti-node points where particle motion is equal to twice the amplitude of a single wave. As can be seen from here, the force acting under this wave model is the drag force. In the stationary wave model, displacement and pressure are expressed by equation (3.3) and (3.4) [74].

$$y(x,t) = A_{SW} \cdot \cos(\omega t) \cdot \sin(kx) \tag{3.3}$$

$$p(x,t) = -p_{SW} \cdot \cos(\omega t) \cdot \cos(kx) \tag{3.4}$$

Here $A_{SW}$ and $p_{SW}$ are the expression of the sum of the amplitudes of the overlapping waves. As can be seen from these equations, there is a 90 ° phase difference between displacement and pressure. Therefore, the points where the displacement is low correspond to the points where the pressure is high and the points where the pressure is high corresponded to the points where the pressure is low.

$$y(x,t) = A \cdot \sin(wt - kx) \tag{3.5}$$

The basis of the acoustic force theory emerged in 1934, when Louis Vessot King calculated the acoustic force acting on a rigid sphere suspended in a non-viscous liquid [75]. This work was later expanded by the calculation of the axutic force acting on the compressible spheres of Yosioka and Kawasima [76]. The model used for cell-like spherical structures is generally the expression developed by Yosioka and Kawasima and shown in (3.6). Here, the expression $\phi(\beta,\rho)$ is developed to compare the compressibility of the acoustic waves between the two environments and is explicitly expressed in equation (3.7).

$$F_{ax} = -\left(\frac{\pi p_0^2 V_p \beta_m}{2\lambda}\right) \cdot \phi(\beta,\rho) \cdot \sin(2kx) \tag{3.6}$$

$$\phi(\beta,\rho) = \frac{5\rho_p - 2\rho_m}{2\rho_p + \rho_m} - \frac{\beta_p}{\beta_m} \tag{3.7}$$

Here, the density of the medium and the particle are expressed as $\rho_m$ and $\rho_p$ and their compressibility as $\beta_m$ and $\beta_p$. Also, $V_p$ is the volume of the particle, and $x$ is the distance from the nearest pressure node.

### 3.2.2 Creating the Cell Mechanical Model

In order to calculate the effect of acoustic force on the cell, a mechanical model of the cell must be created. Although the cell has a very complex structure, where many different organelles and structures come together, a simpler mechanical model needs to be created in order to analyze cell deformation and movements. For this purpose, cell models are generally created by making quite simplifying assumptions. There are many different models developed for different

applications, but the purpose of our project is to measure the stiffness of the cell, which has led us to use models where the cell is assumed to be an elastic material. The models used will be described in this section.

#### 3.2.2.1 Linear viscoelastic solid model

The linear viscoelastic solid model models the whole cell as a homogeneous linear viscoelastic solid as seen in Figure 3.9. This model was developed by Schmid and Schoenlein in 1981 to model the deformation of leukocytes during micro-aspiration. In this model, due to the elasticity of the cell membrane, it is expressed as an elastic (spring) element that absorbs ultrasonic energy, while the cell fluid is expressed as a moving viscous (damping) element. The second spring element can be given as the mass of the cell nucleus. Thus, the effect of the wave produced from an ultrasonic source on the cancer cell can be examined. Constitutional equation used for this model is as seen in (3.8).

$$\tau_{ij} + \frac{\mu}{k_2}\tau_{ıȷ} = k_1\gamma_{ıȷ} + \dot{\mu}\left(1 + \frac{k_1}{k_2}\right)\dot{\gamma_{ıȷ}} \tag{3.8}$$

Here $k_1$, $k_2$ and $\mu$ this refer to the elastic and viscous constants shown in the Figure 3.9. The expression of displacement can be found using this equation.

$$\delta(t) = \frac{F}{8R_1k_1}\left[1 + \left(\frac{k_1}{k_1+k_2} - 1\right)e^{-\frac{t}{\tau}}\right]H(t) \tag{3.9}$$

Thus, a relationship can be established about the cell viscoelastic structure through the wave patterns that will occur in the cell exoskeleton structure due to cell displacement at different frequency values.

#### 3.2.2.2 Maxwell model

The viscoelastic solid model is a useful model for analyzing large deformations on the cell. However, it is insufficient to model smaller and superficial deformations. Constitutional equation used in this model is as seen in equation (3.10).

$$\tau_{ij} + \frac{\mu}{k}\dot{\tau}_{ij} = \mu\dot{\gamma}_{ij} \tag{3.10}$$

Here $k$ is an elastic constant and $\mu$ is a viscous constant. The cell model created in this way is more suitable for expressing small deformations that have a superficial and elastic characteristic.

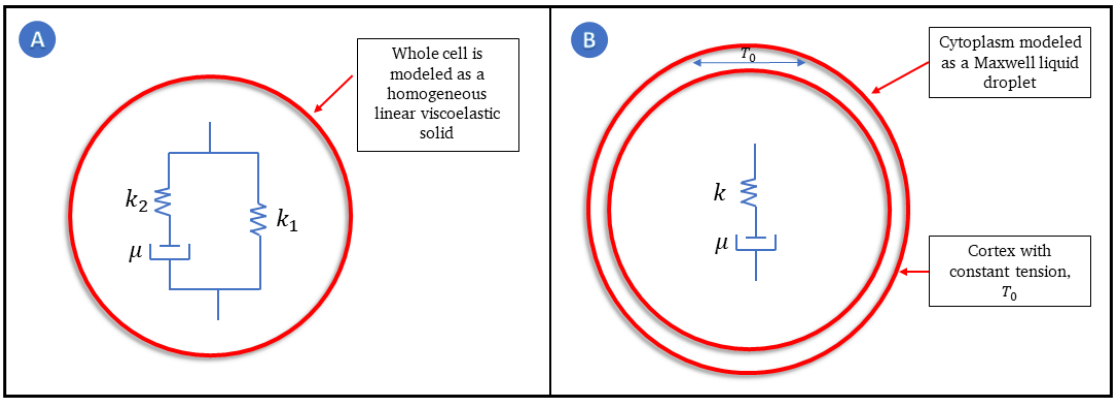


**Figure 3.9** Mechanical models used to predict cell behavior under acoustic waves. The model seen in Figure A is the linear viscoelastic solid model and is used for the analysis of large deformations on the cell. The deformation caused by the drag force that the static waves will create on the cell will be analyzed using this model. The model seen in Figure B is the Maxwell droplet model. It is a model suitable for the analysis of smaller, superficial, and elastic deformations. This model will be used for the analysis of deformations that immersion transducers will form on the cell membrane.

Thanks to the mathematical models created above, the effect of acoustic force on the cell was calculated with the help of experimental results. Consequently, modeling of the cell mechanics has great potential to provide a new attitude on pathologies and biological research questions.

### 3.2.3 Installation of Acoustic Experimental Setup

In order to obtain forces that can deform the surface of the cell, it is necessary to create three-dimensional standing waves in the cell environment. It is necessary to establish a sensitive experimental setup. The experimental setup has been developed to capture this sensitivity. In the developed experimental setup, PZTs with different bandwidths and frequency ranges have been used to create deformation on the cell.

Before the experimental setup was installed, piezo transducers were selected to provide deformation on the cell. As can be seen in Table 3.1, PZTs were used in different mods, frequency ranges and with different resonance frequencies. Among the PZTs used, PZT was the piezo transducer in the first line, where we had the best deformation on the cell. The selected PZT has a frequency in the range between 1Hz and 2KHz and it has Bimorph mode. The deformation created on the cell during the experiments was best observed in this frequency range.

**Table 3.1** Images and operating frequency ranges of PZT used in experiments

| Picture | Definement | Model | Resonant Frequency | Resonant impedance |
|---|---|---|---|---|
|  | Piezo Ceramic Bimorph 40x10x0.5mm 2 KHz | SMBA4510T05M | 2 KHz ± 5% | Maximum Input Voltage: 100 Vpp |
|  | Piezo Bimorph Actuator 25×7.1×0.50mm | SMBA25W7T05PV | Displacement: 0.05mm @ 24 Vpp | Displacement: 0.05mm @ 24 Vp-p |
| 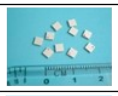 | Piezo Ceraminc Plate 3x3x0.55mm 3.8 MHz | SMPL3W3T05410 | 3.8 MHz ± 5% | Zm: ≤25 Ω |
|  | Piezoelectric Plate Gold Plated | SMPL4X4T311AU | 19MHz ± 5% | |
|  | PZT Ceramic Plate 6x5x0.55mm 3.65 MHz | SMPL6W5T05410 | 3.65 MHz ± 3% | Zm: ≤7.3 Ω |
|  | Surface acoustic wave Piezo Plate 10x2x0.4mm | SMSAW10L2T04RPT | 5.5 MHz ± 3% | Zm: ≤2.2 Ω |
|  | Surface acoustic wave Piezo Plate 14x2x0.4mm | SMSAW14L2T04RPT | 5.4 MHz ± 3% | Zm: ≤6 Ω |
|  | PZT Surface acoustic wave Plate 8.3x2x0.4mm | SMSAW8L2T04RPT | 5.53 MHz ± 3% | Zm: ≤10 Ω |
| 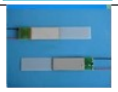 | Piezoelectric Fan Blade 60 Hz | SMPF73W12F60 | 60 Hz ± 2% | Working Voltage: 110V AC |

The operating voltages of the PZT used are up to 100 Vpp. Since the stable working conditions required for precise measurement in the thesis are of great importance, and experimental setup has been created accordingly. In this context, the WMA-300 amplifier of the Falco brand was used in the experiments. WMA-300 is a high voltage, wide bandwidth amplifier. WMA-300 can be used for MEMS activation, EO-modulators, PZT (piezo) positioners, ultrasonic and many other

applications. After the system became more stable, cancer cells belonging to different cell lines were tested in the microfluidic channel. Experiments were made integrated to the holographic system and the optimum frequency range was recalculated.

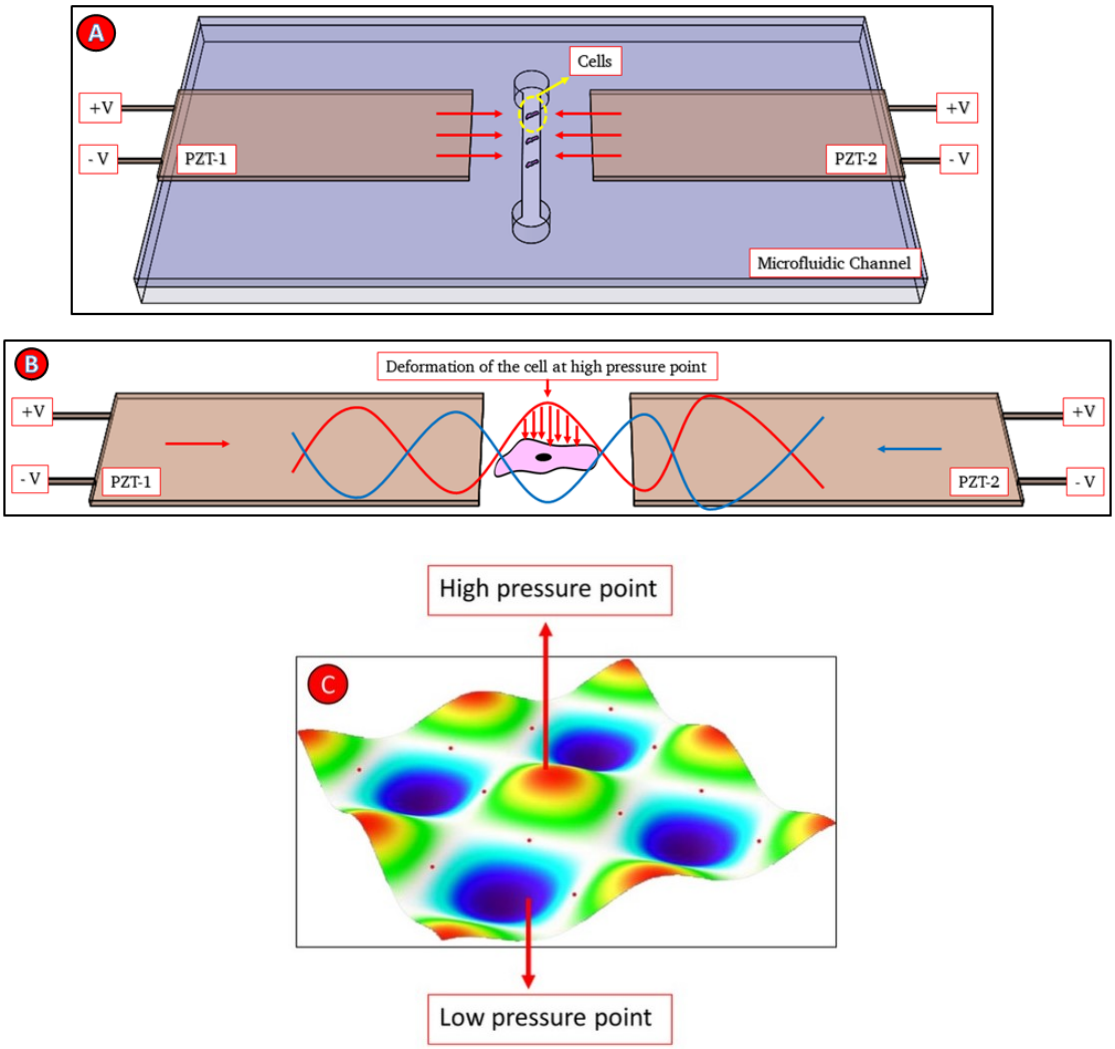


**Figure 3.10** The PZT transducer shown is placed adjacent to the microfluidic device in which the cells were cultured. PZT transducer is used to generate surface waves which in turn generate a deformation force on the cells.

As can be seen from Figure 3.10 acoustic standing wave is generated within the microfluidic channel. The standing wave creates a multi-dimensional acoustic field. Acoustic radiation force exceeds drag and gravity force, thereby trapping and aligning cells in the 3D pressure nodes of standing wave.

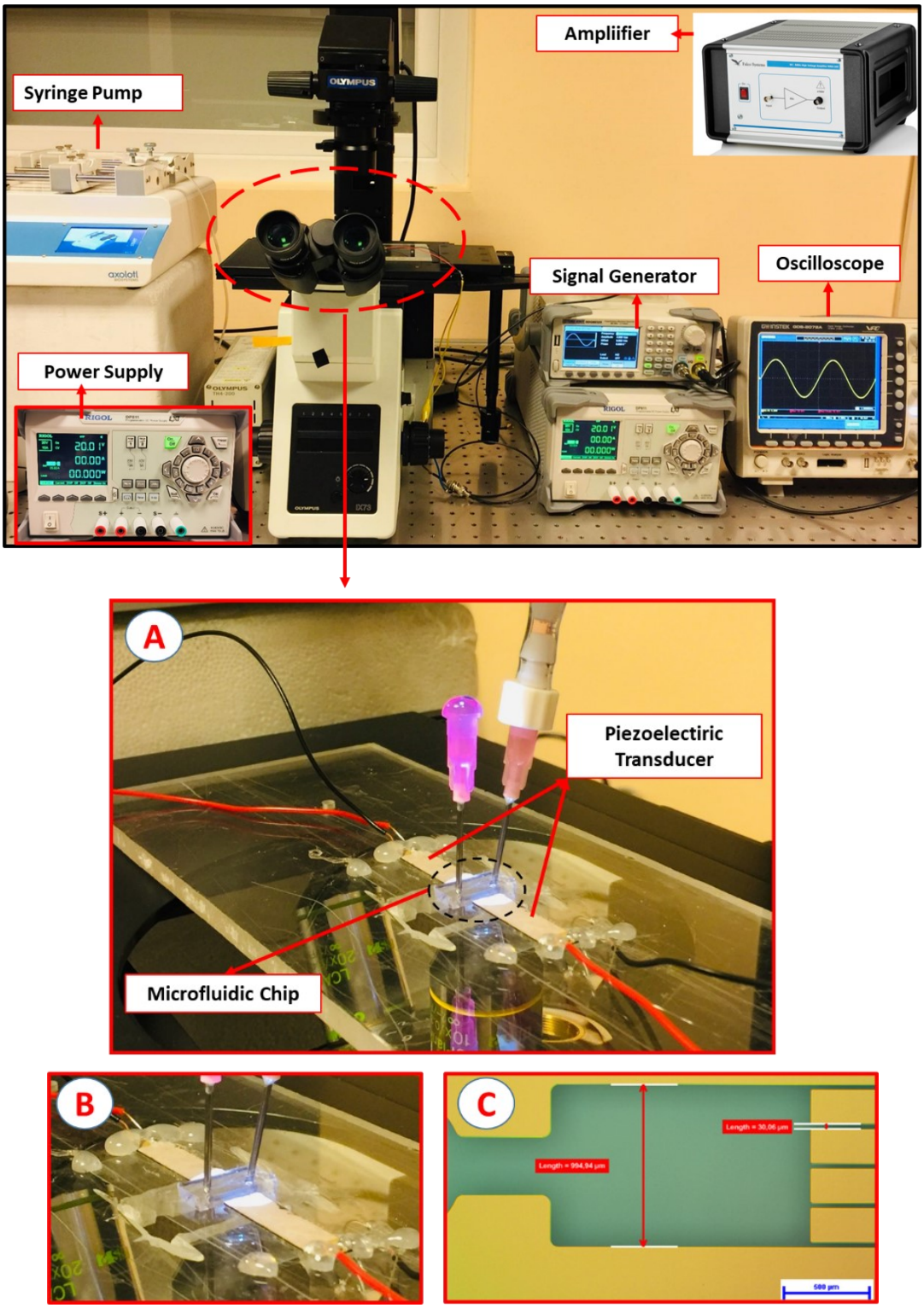


**Figure 3.11** Experimental Setup of Acoustic System. The experimental setup used during the acoustic experiments are shown. The oscilloscope is used to determine the frequency at which the surface waves are generated with highest amplitude. The signal generator is used to generate a sinusoidal signal that is fed into the acoustic transducer through a voltage amplifier. **Figure 3.11.A** The PZT

transducer shown is placed adjacent to the microfluidic device in which the cells were cultured. PZT transducer is used to generate surface waves which in turn generate a deformation force on the cells. A thick layer of PDMS (1:10 silicone elastomer and curing agent) was used to prevent the vibration of PZT transducers to affect the imaging setup.

Finally, the acoustic surface waves created using piezo were increased with the help of an Falco WMA-300 model amplifier, which converts electrical energy into a mechanical vibration, to be in contact with the channel measuring piezo shown in Figure 3.11, which can operate at between 1 Hz to 1Khz frequencies.

### 3.2.4 Results and Discussion

Mechanical properties of the cancer cell is a critical parameter for pharmacy and biological research. Cell morphology is an important determinant of the cell genotype and determines many of its characteristics including its surface adhesion behavior its intracellular signaling pathway regulation and its membrane permeability. It is also a stronger indicator of the class a cell belongs to, compared to classical light microscopy techniques [77-80].

Within the scope of the thesis, the acoustic mechanical effect acting on the cancer cell was measured with a holographic imaging system. The holographic imaging method, algorithms used, and the results obtained during an experiment in which cell cultures in microfluidic device. The motive of this study is to show the advantages of quantitative phase imaging methods where the observation of morphological transformation of the cell. During the EMT phase, cancer cells lose their adhesive nature and morph into a mesenchymal state in which they start migrating through the blood stream into different parts of the body as circulating tumor cells. Observation of the transformation of surface structure in 3D during the EMT phase is critical for better understanding the factors that trigger it since many of its precursors manifests itself in cell morphology. Accurate depth information obtained through quantitative phase imaging methods could play a key role in understanding the dynamics of this complex process. Holographic imaging apparatus consists of a phase shifting inline Mach-Zehnder interferometer coupled to a spatial light modulator used for phase retardation. As a coherent light

source, we use a 521 nm, 10mW DPSSL laser. Phase-shifting is achieved through the use of a high frequency piezo actuator actuated in 500 steps per second. We developed an algorithm for real-time holographic reconstruction using a continuously shifting piezo actuator and a high-speed CCD camera. For each frame we predict the phase difference between last two consecutive frames and use the last period of the captured interferograms for holographic reconstruction.

Our method is particularly advantageous for cell cultures where the present fluid flow creates transient deformations in the fringe patterns. To further lower the noise due to commonly used microfluidic device. And then we compare different noise reduction strategies and propose a novel noise reduction strategy based on the BM3D method which gives superior performance for dynamical cell cultures. We then apply a watershed transform based super pixel segmentation algorithm to continuously track the morphological evolution of individual cells during acoustic effect. Our method allows us to capture reconstruction at 20 FPS in real-time. The demonstrated application clearly shows that holographic imaging techniques present valuable information that gives insights into the physiological underlying of behavioral patterns cancer cells typically undergo.

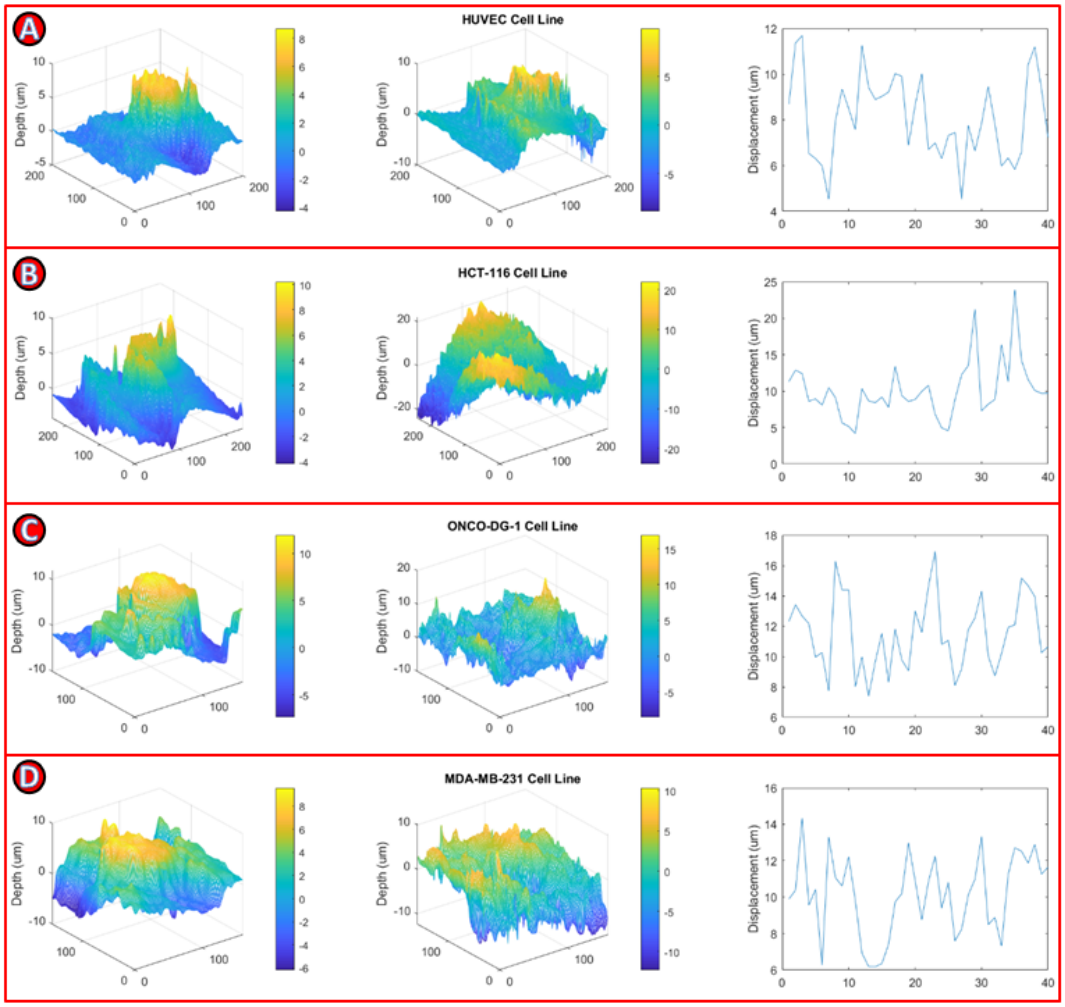


**Figure 3.12** The deformation of the HCT-116 (Colon Cancer), MDA-MB-231 (Breast Cancer), ONCO-DG-1 (Ovarian Cancer), and HUVEC (Human Umbilical Vein Endothelial) cells under the acoustic effect.

PZTs used in the experiments were used in sinusoidal wave mode and 3Vpp amplitude. For the optimum frequency range, 1Hz, 5Hz, 10 Hz and 1 KHz are selected. In these frequency ranges, the cells were exposed to acoustic effect at the determined frequency ranges for 10 seconds. The acoustic effect occurring on the cells have been calculated with the holographic experimental setup on the surface in 3-dimensions.

As mentioned in the previous sections, cancer cells have a less stiff than healthy cells, as is known from the literature.

As can be seen in Figure 3.12A, when the HUVEC cell line is treated as a healthy cell, the deformation on the cell is ± 5 $\mu$m. Figure 3.12 B shown that the

deformation occurring in the range between 1Hz and 1Khz on the HCT-116 (Colon Cancer) cell line is ± 20 $\mu$m. The deformation on the ONCO-DG-1 (Ovarian Cancer) cell line shown in Figure 3.12 C in the range of 1Hz to 1Khz is ± 15 $\mu$m. The deformation on the MDA-MB-231 (Breast Cancer) cell line shown in Figure 3.12 C in the range of 1Hz to 1Khz is ±10 $\mu$m.

These results show that cancer cells have different stiffness values in themselves. At the same time, these results obtained holographically confirm the information obtained in the literature. Although all cell lines are exposed to the same frequencies and amplitudes, deformations occurring on their surfaces are different from each other due to differences in cell structures.

# 4
# RESULTS AND DISCUSSION

This thesis aims to microfluidic systems have been developed to determine the mechanical properties of cancer cells and healthy cells as a single cell with a holographic imaging technique. The most important innovations brought by developed microfluidic chips are that it can perform many operations at the same time, observing cell migration, detection of mechanical stiffness of cells, and the microchannels can be continuously identified and followed. They also provide a suitable environment for processing and analyzing cells in a narrow and restricted area. In the microfluidic systems developed within the scope of the thesis PDMS based microchips are produced and designed as a platform in which microchannels are contained, the cells can be immobilized individually and exposed to acoustic effects. HCT-116 (Colon Cancer), ONCO-DG-1 (Ovarian Cancer), MDA-MB-1 (Mammary Cancer) were chosen as the appropriate cancer cell line and HUVECs (Human Umbilical Vein Endothelial Cells) selected as a healthy cell line for the experiments.

To understand the microfluidic system, we start with a discussion of how physical effects manifest at the microscale. In the first part of the thesis, we developed a microflow sensor prototype with zero mechanical contact in a microfluidic channel via diamagnetic levitation. And then, we also describe the fabrication of microfluidic platforms for the detection of single-cell mechanical properties. The culturing of cancer cells to be used during the experiments and their integration into the microfluidic system are also described. In the third section of the thesis describe the application of developed microfluidic system for cancer cell mechanical properties detection.

Thesis results show that cancer cells have different stiffness values in themselves. At the same time, these results obtained holographically confirm the information obtained in the literature. Although all cell lines are exposed to the same

frequencies and amplitudes, deformations occurring on their surfaces are different from each other due to differences in cell structures.

Therefore, the mechanical properties of cancer cells can be used as new diagnostic and / or prognostic markers to complete the histological examinations and genetic phenotyping of the tumor. Many studies investigating the mechanics of healthy and cancer cells have found that cancer cells have less stiffness than healthy cells. More importantly, the reduction in stiffness correlates with the progression of the disease. Cell stiffness is not the only physical parameter changed in cancer cells. Cell adhesion, traction forces, or sigh stresses are also affected. The results we obtained as a result of the thesis are of great importance for cancer treatment and pharmacological drug trials, which are among the biggest problems of today.

# REFERENCES


[1] H. J. Yoon, J.M. Jung, J.S. Jeong, and S.S. Yang, " Micro devices for a cerebrospinal fluid (CSF) shunt System," Sens. Actuators A, Phys., vol. 110, No. 1-3, pp. 68-76, Feb. 2004.

[2] F. Hedrich, K. Kliche, M. Storz, S. Billat, M. Ashauer, and R. Zengerle,. “Thermal flow sensors for MEMS spirometric devices,” Sensors. Actuators A Phys., vol. 162, no. 2, pp. 373–378, 2010.

[3] H. Kuttner, G. Urban, A. Jachimowicz, F. Kohl, F. Olcaytug, P.Goiser, “Microminiaturized thermistor arrays for temperature gradient,flow and perfusion measurements,” Sens. Actuators, A 25–27_1991. 641–645.

[4] Y.S. Lee, K.D. Song, J.S. Huh, W.Y. Chung and D.D. Lee, “Fabrication of clinical gas sensor using MEMS process,” Sens. Actuators B: Chem. 108 (2005) 292-297.

[5] T. S. J. Lammerink, N. R. Tas, M. Elwenspoek and J. H. J. Fluitman, “Micro-liquid flow sensor”, Sensors and Actuators. A, Vol.37/38, pp.45–50, 1993.

[6] G. Kaltsas, and A. G. Nassiopoulou. "Gas flow meter for application in medical equipment for respiratory control: study of the housing." Sensors and Actuators A: Physical 110.1-3 (2004): 413-422.

[7] Y. Ma, S. Ma, T. Wang, W. Fang, “Air-flow sensor and humidity sensor application to neonatal infant respiration monitoring,” Sens. Actuat. A: Phys. 1995, 47-50

[8] K. C. Katuri, S. Asrani, and M. K. Ramasubramanian, “Intraocular pres-sure monitoring sensors,” IEEE Sensors J., vol. 8, no. 1, pp. 12–19, Jan. 2008

[9] D.L. Polla, A.G. Erdman, W.P. Robbins, D.T. Markus, J. Diaz-Diaz., R. Rizq, Y. Nam, H.T. Brickner, “Microdevices in medicine, Annu.” Rev. Biomed. Eng., 2:551, 2000.

[10] H. Ceylan, J. Giltinan, K. Kozielski, M. Sitti. Mobile microrobots for bioengineering applications. Lab on a Chip, vol. 17, no. 10, pp. 1705–1724, 2017. DOI: 10.1039/C7LC 00064B.

[11] B. J. Nelson, I. K. Kaliakatsos, J. J. Abbott. “Microrobots for minimally invasive medicine,” Annual Review of Biomedical Engineering, vol. 12, pp. 55–85, 2010. DOI: 10.1146/annurev-bioeng-010510-103409.

[12] M. Hagiwara, T. Kawahara, Y. Yamanishi, and F. Arai, "Driving Method of Microtool by Horizontally-arranged Permanent Magnets for Single Cell Manipulation", Applied Physics Letters, vol. 97, pp. 013701-1-013701-3, 2010.

[13] G. Lucarini, V. Iacovacci, P.J. Gouveia, L. Ricotti, A. Menciassi, “Design of a novel magnetic platform for cell manipulation,” J Micromech Microeng. 28: 025009 (2018)

[14] KE Peyer, L Zhang, BJ Nelson, “Bio-inspired magnetic swimming microrobots for biomedical applications,” Nanoscale 5 (4), 1259-1272, 2013. 472, 2013.

[15] S. Fusco, H.-W. Huang, K. E. Peyer, C. Peters, M. Häberli, A. Ulbers, et al., "Shape-Switching Microrobots for Medical Applications: The Influence of Shape in Drug Delivery and Locomotion," ACS Appl. Mater. Interfaces, vol. 7, pp. 6803-6811, 2015/04/01 2015.

[16] M. Hagiwara, T. Kawahara, Y. Yamanishi, T. Masuda, L. Feng, F. Arai, “High performance magnetically driven microtools with ultrasonic vibration for biomedical innovations,” In Proceedings of the 2011 IEEE International Conference on Robotics and Automation (ICRA), Shanghai, China, 9–13 May 2011; pp. 3453–3454.

[17] F. Tendick, S. S. Sastry, R. S. Fearing, and M. Cohn, “Applications of micromechatronics in minimal invasive surgery,” IEEE Trans. Mechatronics, vol. 3, no. 1, pp. 34–42, Mar. 1998.

[18] SE Chung, X Dong, M Sitti, “Three-dimensional heterogeneous assembly of coded microgels using an untethered mobile microgripper,” Lab on a Chip 15, 1667–1676, 2005.

[19] B. Profijt, C. Pigot, G. Reyne, R. M. Grechishkin, and O. Cugat, “Stable diamagnetic self-levitation of a micro-magnet by improvement of its magnetic gradients,” J. Magn. Magn. Mater. 321, 259–262, 2009.

[20] H. Uvet, A.A. Demirçali, Y. Kahraman, R. Varol, T. Kose, K. Erkan, "Micro-UFO (Untethered Floating Object): A Highly Accurate Microrobot Manipulation Technique", MICROMACHINES, vol.9, pp.1-20, 2018

[21] S. Silvestri and E. Schena, “Micromachined Flow Sensors in Biomedical Applications,” Micromachines, vol. 3, no. 2, pp. 225–243, Mar. 2012.

[22] A. Glaninger, A. Jachimowicz, F. Kohl, R. Chabicovsky, and G. Urban, “Wide range semiconductor flow sensors,” Sens. Actuators A Phys. 85(1-3), 139–146 (2000).

[23] W. Hilber, S. Clara and B. Jakoby, "Sensing Physical Fluid Properties in Microcavities Utilizing Diamagnetic Levitation," in IEEE Transactions on Magnetics, vol. 51, no. 1, pp. 1-4, Jan. 2015.

[24] S. Clara, et al. "A viscosity and density sensor based on diamagnetically stabilized levitation." IEEE sensors journal 15.3: 1937-1944, 2014.

[25] J. Abadie, E. Piat, S. Oster, M. Boukallel,”Modeling and experimentation of a passive low frequency nano force sensor based on diamagnetic levitation,” Sensors and Actuators A: Physical, Volume 173, Issue 1, 2012, Pages 227

[26] D. Garmire, et al. "Diamagnetically levitated MEMS accelerometers." TRANSDUCERS 2007-2007 International Solid-State Sensors, Actuators and Microsystems Conference. IEEE, 2007.

[27] W. Thomson, “On the forces experienced by small spheres under magnetic influence; and on some of the phenomena presented by diamagnetic substances,” Cambridge Dublin Math. J., May 1847

[28] H. Boerdijk, “Levitation by static magnetic fields,” Philips Tech. Rev., vol. 18, pp. 125–127, 1956

[29] M.D., Simon, L. O. Heflinger, and A. K. Geim. "Diamagnetically stabilized magnet levitation." American journal of physics 69.6: 702-713, 2001

[30] R. E. Pelrine, (2004). Diamagnetic Levitation: Known since the 1930s, a simple technique for suspending objects magnetically is just now finding practical application. American scientist, 92(5), 428-435.

[31] Y., Taitel, A. E. Dukler. "A model for predicting flow regime transitions in horizontal and near horizontal gas-liquid flow."AIChE journal 22.1: 475, (1976)

[32] B.C., Sakiadis, "Boundary-layer behavior on continuous solid surfaces: I. Boundary-layer equations for two-dimensional and axisymmetric flow." AIChE Journal 7.1: 26-28, 1961

[33] R.D., Waldron, "Diamagnetic levitation using pyrolytic graphite." Review of Scientific Instruments 37.1 (1966): 29-35.

[34] A.A., Demirçali, K., Erkan, H., Uvet, "A Study on Finding Optimum Parameters of a Diamagnetically Driven Untethered Microrobot", JOURNAL OF MAGNETICS, vol.22, pp.539-549, 2017

[35] R. B. Payne, "Calculations of unsteady viscous flow past a circular cylinder." Journal of Fluid mechanics 4.1: 81-86, 1958

[36] M.E. Hoque, T. Mizuno, "Magnetic levitation technique for active vibration control." Magnetic Bearings, Theory and Applications. InTech, 2010.

[37] C. Elbuken, M. B. Khamesee, and M. Yavuz. "Eddy current damping for magnetic levitation: downscaling from macro-to micro-levitation." Journal of Physics D: Applied Physics 39.18: 3932, 2006

[38] T. Morita, K. Shimizu, M. Hasegawa, K. Oka, and T. Hoguchi, “A Miniaturized Levitation System with Motion Control Using a Piezoelectric Actuator,” IEEE Trans. on Control Systems Technology, Vol.10, No.5, pp. 666-670, 2002.

[39] H.A. Sodano, J.S. Bae, “Eddy current damping in structures. Shock and Vibration,” Digest, 36(6), 469, 2004.

[40] D. Simon, M & O. Heflinger, L & Ca, Torrance & K. Geim, A. (2001). Diamagnetically stabilized magnet levitation. American Journal of Physics - AMER J PHYS. 69. 10.1119/1.1375157Publications from the thesis

[41] H. Ceylan, J. Giltinan, K. Kozielski, M. Sitti. Mobile microrobots for bioengineering applications. Lab on a Chip, vol. 17, no. 10, pp. 1705–1724, 2017.

[42] B. J. Nelson, I. K. Kaliakatsos, and J. J. Abbott, "Micro-robots for minimally invasive medicine," Annu. Rev. Biomed. Eng., vol. 12, pp. 55–85, Aug. 2010.

[43] M. Hagiwara, T. Kawahara, Y. Yamanishi, and F. Arai, “Driving method of microtool by horizontally arranged permanent magnets for single cell manipulation,” Appl. Phys. Lett. 97, 013701. 13, 2010.

[44] G. Lucarini, V. Iacovacci, P.J. Gouveia, L. Ricotti, and A. Menciassi, “Design of a novel magnetic platform for cell manipulation,” J. Micromech. Microeng. 28, 14, 2018.

[45] K. E. Peyer, L. Zhang, and B. J. Nelson, “Bio-inspired magnetic swimming microrobots for biomedical applications,” Nanoscale, vol. 5, no. 4, pp. 1259–1272, 2013.

[46] S. Fusco, H.-W. Huang, K. E. Peyer, C. Peters, M. Häberli, A. Ulbers, A. Spyrogianni, E. Pellicer, J. Sort, S. E. Pratsinis, B. J. Nelson, M. S. Sakar, and S. Pané, “Shape-switching microrobots for medical applications: The influence of shape in drug delivery and locomotion,” ACS Appl. Mater. Interfaces 7, 6803–6811 (2015).

[47] M. Hagiwara, T. Kawahara, Y. Yamanishi, T. Masuda, L. Feng, F. Arai, “High performance magnetically driven microtools with ultrasonic vibration for biomedical innovations,” In Proceedings of the 2011 IEEE International Conference on Robotics and Automation (ICRA), Shanghai, China, pp. 3453–3454. 17, 9–13 May 2011.

[48] F Tendick, SS Sastry, RS Fearing, M Cohn, “Applications of micromechatronics in minimally invasive surgery,” IEEE/ASME Trans. Mechatron. 3(1):34–42, 1998

[49] S. E. Chung, X. Dong, and M. Sitti, “Three-dimensional heterogeneous assembly of coded microgels using an untethered mobile microgripper,” Lab Chip, 15, 1667– 1676, 2015.

[50] H. B. Profijt, C. Pigot, G. Reyne, R. M. Grechishkin, and O. Cugat “Stable diamagnetic self-levitation of a micro-magnet by improvement of its magnetic gradients,” J. Magn. Magn. Mater. 321, 259–262, 2009.

[51] A. Gosain, LA. DiPietro, “Aging and wound healing,” World J Surg 28:321-326, 2004.

[52] K.P. Goetsch, K.H. Myburgh, U. Niesler "In vitro myoblast motility models: investigating migration dynamics for the study of skeletal muscle repair." *Journal of muscle research and cell motility* 34.5, 333-347, 2013

[53] M. Fronza, et al. "Determination of the wound healing effect of Calendula extracts using the scratch assay with 3T3 fibroblasts." *Journal of ethnopharmacology* 126.3: 463-467, 2013

[54] Y. Zhang, CW. Lo, JA. Taylor, S. Yang “Replica molding of high-aspect-ratio polymeric nanopillar arrays with high fidelity,” Langmuir. 22:8595–8601, 2006

[55] A. Pavesi, et al. "Engineering a 3D microfluidic culture platform for tumor-treating field application." *Scientific reports* 6: 26584, 2006

[56] II. George Broughton, J.E. Janis, C.E. Attinger, “The basic science of wound healing,” Plastic and Reconstructive Surgery 117 (7S), 12S-34S, 2006. 1200, 2006.

[57] N.B Menke, K.R Ward, T.M Witten, D.G Bonchev, R.F Diegelmann, “Impaired wound healing,” Clinics in dermatology 25 (1), 19-25, 2007.

[58] A. D. Van Der Meer, K. Vermeul, A. A. Poot, J. Feijen, and I. Vermes, “A microfluidic wound-healing assay for quantifying endothelial cell migration,” American Journal of Physiology-Heart and Circulatory Physiology, 298(2), H719-H725, 2009.

[59] A. D. Castiaux, D. M. Spence, R. S. Martin, “Review of 3D cell culture with analysis in microfluidic systems,” *Analytical Methods*, *11*(33), 4220-4232, 2019

[60] S. Torino, B. Corrado, M. Iodice, G. Coppola, “Pdms-based microfluidic devices for cell culture,” *Inventions*, *3*(3), 65, 2018

[61] S. Kim, A. Ghanbari,nB. J. Nelson, H. Choi, “Fabrication and characterization of magnetic microrobots for three-dimensional cell culture and targeted transportation,” *Advanced Materials*, *25*(41), 5863-5868, 2013

[62] XJ Li, AV Valadez, P Zuo, Z Nie, “Microfluidic 3D cell culture: potential application for tissue-based bioassays,” *Bioanalysis*, *4*(12), 1509-1525, 2012

[63] M. Ravi, V. Paramesh, S.R. Kaviya, E. Anuradha, F.D.P Solomon, “3D cell culture systems: advantages and applications,” *Journal of cellular physiology*, *230*(1), 16-26, 2015

[64] H. Lee and Y.P.P. Chen, “Cell morphology-based classification for red cells in blood smear images,” Pattern Recognition Letters, vol. 49, pp. 155 – 161, 2014.

[65] I. Yamaguchi, and T. Zhang, “Phase-shifting digital holography,” Optics letters 22.16: 1268-1270, 1997

[66] T. Latychevskaia, and H.W. Fink, “Practical algorithms for simulation and reconstruction of digital in-line holograms,” Applied optics 54.9: 2424-2434, 2015

[67] A. Schwartz, et al. “Standardizing flow cytometry: A classification system of fluorescence standards used for flow cytometry,” Cytometry, vol. 33, no. 2, pp. 106–114, 1998.

[68] A. Ciurte, C. Selicean, O. Soritau, and R. Buiga, “Automatic detection of circulating tumor cells in darkfield microscopic images of unstained blood using boosting techniques,” PLOS ONE, vol. 13, no. 12, pp. 1–11, 12 2018.

[69] D. Yang and Y. Ai, “Microfluidic impedance cytometry device with n-shaped electrodes for lateral position measurement of single cells/particles,” Lab Chip, vol. 19, pp. 3609–3617, 2019.

[70] M. Hejna, A. Jorapur, J. S. Song, and R. L. Judson, “High accuracy label-free classification of single-cell kinetic states from holographic cytometry of human melanoma cells,” Scientific Reports, vol. 7, no. 1, p. 11943, 2017.

[71] Y. Xia, Y. Gao, B. Wang, H. Zhang, and Q. Zhang, “Optimizing the method of cell separation from bile of patients with cholangiocarcinoma for flow cytometry,” Gastroenterology research and practice, vol. 2019, 2019.

[72] E. M. Strohm and M. C. Kolios, “Classification of blood cells and tumor cells using label-free ultrasound and photoacoustics,” Cytometry Part A, vol. 87, no. 8, pp. 741–749, 2015.

[73] C. Allayous, S. Regis, A. Bruel, D. Schoevaert, R. Emilion, and T. Marianne-Pepin, “Velocity allowed red blood cell classification,” in 10th International IFAC Symposium on computer applications in biotechnology, vol. 1, 2007.

[74] A. Gosain, LA. DiPietro, “Aging and wound healing,” World J Surg 28:321-326, 2004

[75] K. P. Goetsch, K. H. Myburgh, and U. Niesler, “In vitro myoblast motility models: investigating migration dynamics for the study of skeletal muscle repair,” *Journal of muscle research and cell motility* 34.5-6: 333-347, 2013

[76] X. Ding, Z. Peng, S.-C. S. Lin, M. Geri, S. Li, P. Li, Y. Chen,M. Dao, S. Suresh, and T. J. Huang, “Cell separation using tiltedangle standing surface acoustic waves,” Proceedings of the National Academy of Sciences, vol. 111, no. 36, pp. 12 992–12 997, 2014.

[77] J. B. Galper, “Human umbilical vein endothelial cells and human dermal microvascular endothelial cells offer new insights into the relationship between lipid metabolism and angiogenesis,” Stem Cell Reviews, vol. 2, no. 2, pp. 93–101, jun 2006.

[78] A. A. Khalili and M. R. Ahmad, “A Review of cell adhesion studies for biomedical and biological applications,” pp. 18 149–18 184, aug 2015.

[79] A. D. Bershadsky and M. M. Kozlov, “Crawling cell locomotion revisited,” Proceedings of the National Academy of Sciences, vol. 108, no. 51, pp. 20 275–20 276, 2011.

[80] R. Maan, G. Rani, G. I. Menon, and P. A. Pullarkat, “Modeling cellsubstrate de-adhesion dynamics under fluid shear,” Physical biology, vol. 15, no. 4, p. 046006, 2018.

# PUBLICATIONS FROM THE THESIS

**Contact Information:** aydemir.gizem@outlook.com

## Papers

1. G. Aydemir, A. Kosar, and H. Uvet, "Design and Implementation of a Passive Micro Flow Sensor Based on Diamagnetic Levitation," Sensors and Actuators A: Physical, 300, 111621, 2019.
2. H. E. Meco, A. Karadag, S. Omeroglu, G. Aydemir, G. Calibasi Kocal, M. E. Oruc, H. Uvet, Y. Basbinar, "Optimization of Different Surface Modifications for Binding of Tumor Cells in a Microfluidic Systems. Journal of Basic and Clinical Health Sciences," 2019.
3. A. Demircali, R. Varol, G. Aydemir, E. Saruhan, K. Erkan, H. Uvet, "Motion Behaviors of a Microrobot Subject to Liquid Laminar Flow," Transactions on Mechatronics, Under Review.
4. G. Aydemir, R. Varol, S. Omeroglu, A. Demircali, A. Kosar, H. Uvet, "Wound Model Generation on-Chip with the Use of Micro-Robot," Lab-on-Chip, Submitted.
5. G. Aydemir*, M. T. Gevari*, G. Gharib, H. Uvet, M. Ghorbani**, A. Kosar **, "Immobilized cancer cell lines bombardment using spray under the effect of hydrodynamic cavitation," Nature Communications, Submitted.

## Conference Papers

1. G. Aydemir, C. Erozer, and H. Uvet, "Design and Implemantation of Micro Flow Sensor Based on Diamagnetic Levitation,"CEIT, 0.1109/CEIT.2018.875177, Istanbul, 2018.
2. G. Aydemir, B. Calis, K. Erkan, and H. Uvet, "A Study on Micro Flow Sensor Based on Diamagnetic Levitation," International Conference on Manipulation, Automation and Robotics at Small Scales (MARSS), Japan, 2018.
3. G. Aydemir, R. Varol, C. Tatar, E. O. Ustomar, H. Uvet, "A new method for creating a wound model with micro-robot in microfluidic device," International Conference on Manipulation, Automation and Robotics at Small Scales (MARSS), 2020.
4. R. Varol, G. Aydemir, S. Omeroglu, Y. Baspinar, and H. Uvet, "Automated Manipulation of 2D Cell Cultures by Means of Depth Aware Holographic Visual

Feedback," International Conference on Manipulation, Automation and Robotics at Small Scales (MARSS), 2020.

5. R. Varol, E. Saruhan, Z. Orucu, S. Omeroglu, Z. Karavelioglu, G. Aydemir, Y. Basbinar and H. Uvet, "Classification Of Cells Based on Their Drifting Velocity Under Acoustic Radiation Pressure," International Conference on Manipulation, Automation and Robotics at Small Scales (MARSS), 2020.
6. S. Omeroglu, G. Aydemir, R. Varol, G. Karadag, E. Meco, M.E. Oruc, Y. Baspınar, B. Esmer, H. Uvet, "Immobilization of CTCs on Silane-Modified Surfaces," International Cancer Ion Channels Congress, https://doi.org/10.1515/tjb-2019-44s206, Turkey, 2019.
7. R. Varol R, G. Aydemir, A. Karadag, E. Meco, S. Omeroglu, M.E. Oruc, Y. Baspınar, B. Esmer, H. Uvet, "Holographic Imaging of Cell Proliferation" International Cancer Ion Channels Congress, https://doi.org/10.1515/tjb-2019-44s206, Turkey, 2019.
8. R. Varol R, G. Aydemir, S. Omeroglu, A. Karadag, E. Meco, S. Omeroglu, M.E. Oruc, Y. Baspınar, B. Esmer, H. Uvet, "Holographic Imaging of Tumor Cells During Epithelial Mesenchymal Transition," SPIE Photonics Europe, France, 2020.